

# Bent-Shaped *p*-Type Small-Molecule Organic Semiconductors: A Molecular Design Strategy for Next-Generation Practical Applications

Toshihiro Okamoto,\* Craig P. Yu, Chikahiko Mitsui, Masakazu Yamagishi, Hiroyuki Ishii, and Jun Takeya



Cite This: *J. Am. Chem. Soc.* 2020, 142, 9083–9096



Read Online

ACCESS |



Metrics & More



Article Recommendations



Supporting Information

**ABSTRACT:** Significant progress has been made in both molecular design and fundamental scientific understanding of organic semiconductors (OSCs) in recent years. Suitable charge-carrier mobilities ( $\mu$ ) have been obtained by many high-performance OSCs ( $\mu > 10 \text{ cm}^2 \text{ V}^{-1} \text{ s}^{-1}$ ), but drawbacks remain, including low solution processability and poor thermal durability. In addition, since aggregation of OSCs involves weak intermolecular interactions, the molecules are perpetually in thermal motion, even in the solid state, which disrupts charge-carrier transport. These issues limit potential applications of OSCs. The present work examines a molecular design for hole-transporting (*p*-type) OSCs based on the “bent-shaped” geometry with specific molecular orbital configurations, which aims to enhance effective intermolecular orbital overlaps, stabilize crystal phases, suppress detrimental molecular motions in the solid state, and improve solution processability. The results indicated that such OSCs have high  $\mu$  and suitable solution processability, and are resistant to ambient and thermal conditions, making them suitable for practical applications.

## INTRODUCTION

Organic semiconductors (OSCs) are of intense scientific and technological interest due to their potential incorporation in printable and flexible electronics, such as organic field-effect transistors (OFETs),<sup>1–4</sup> organic light-emitting diodes (OLEDs),<sup>5,6</sup> organic photovoltaics (OPVs),<sup>7–11</sup> and organic thermoelectrics (OTE).<sup>12–15</sup> In contrast to their inorganic semiconductor counterparts,<sup>16</sup> the functions of OSCs are governed by intermolecular charge transport between adjacent  $\pi$ -conjugated molecules, molecular geometry, and electronic characteristics.<sup>17–26</sup> Thus, rational, versatile molecular design could lead to the development of high-performance, printable OSCs that are suitable for large-scale industrial production.

The general requirements for printable, flexible electronic devices include (1) high chemical stability under ambient conditions without the need for special precautions, (2) high charge-carrier mobility ( $\mu$ ) that exceeds the performance of conventional amorphous silicon (e.g.,  $0.5\text{--}1.0 \text{ cm}^2 \text{ V}^{-1} \text{ s}^{-1}$ )<sup>27</sup> and is competitive with that of metal-oxide semiconductors, (3) sufficient solubility in common organic solvents that allows low-cost solution processing for device fabrication, (4) high thermal durability (highly stable crystal phase above  $150 \text{ }^\circ\text{C}$  to withstand fabrication processes),<sup>28</sup> and (5) facile synthetic routes for large-scale production.

To date, various molecular designs based on  $\pi$ -conjugated materials have been reported, with the aim of achieving the high performance required for the aforementioned applications.<sup>29–40</sup> Representative molecular designs in the literature have utilized linear or quasi-linear  $\pi$ -electron cores ( $\pi$ -cores) such as pentacene,<sup>41</sup> [1]benzothieno[3,2-*b*][1]benzothiophene (BTBT),<sup>42</sup> and dinaphtho[2,3-*b*:2',3'-*f*]thieno[3,2-*b*]-thiophene (DNNT)<sup>43</sup> as a means of obtaining effective

intermolecular  $\pi$ -orbital overlaps necessary for charge transport in the solid state (Figure 1).<sup>4,44</sup> These  $\pi$ -cores aggregate through multiple intermolecular C–H $\cdots\pi$ , S $\cdots$ S, and S $\cdots\pi$  interactions and form two-dimensional (2D) herringbone (HB)-type packing structures that favor 2D charge carrier transport.<sup>45</sup> Various studies have also focused on side-chain engineering with bulky alkylsilyl,<sup>46,47</sup> linear alkyl,<sup>48–52</sup> and unsymmetrical substituents<sup>53–57</sup> in order to improve the

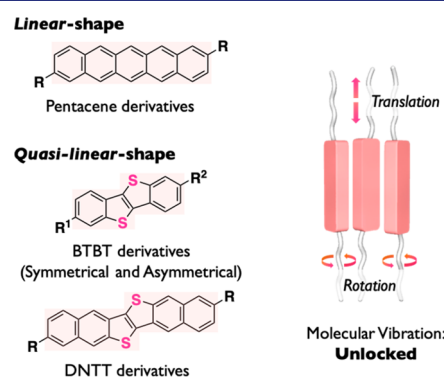


**Figure 1.** Molecular structures of representative organic semiconductors.

Received: September 27, 2019

Published: April 15, 2020



solubility and tune the aggregated structures of these  $\pi$ -cores (Figure 1). As a result, high-performance and solution-processable OSCs with these substituted  $\pi$ -cores having excellent  $\mu$  ( $>10 \text{ cm}^2 \text{ V}^{-1} \text{ s}^{-1}$ ) have been reported.<sup>58–60</sup> However, both linear and quasi-linear alkyl-substituted  $\pi$ -cores have exhibited phase transitions from crystalline to liquid crystalline or other crystal phases at temperatures around 90–130 °C,<sup>42,61–63</sup> leading to degradation of transistor performance at elevated temperatures during device fabrication. It has also been recently reported that unsymmetrical substituted BTBT analogues aggregate to form a highly crystalline liquid crystal phase.<sup>53</sup> These challenges associated with various representative OSCs illustrate that it is still difficult to simultaneously achieve sufficient solubility, thermal durability, and high  $\mu$  with conventional molecular design strategies based on OSC  $\pi$ -cores.

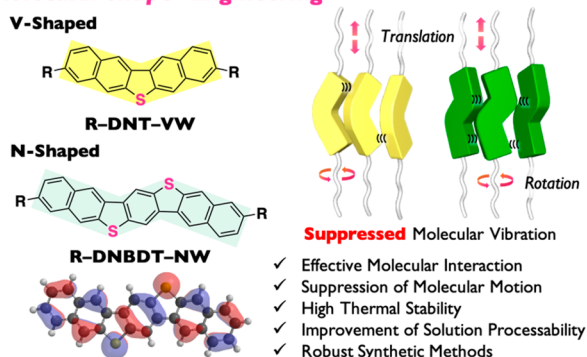
Recently, several fascinating studies have been reported concerning the detrimental effects of large-amplitude molecular motions on the performance of high-mobility OSCs such as pentacene and BTBT derivatives.<sup>64–67</sup> Sirringhaus and co-workers also suggested that the dynamic disorder of OSCs in the solid state might be the parameter having the most harmful effect on charge transport.<sup>67</sup> Hence, it is apparent that future rational molecular design not only should be guided by intramolecular characteristics or intermolecular orbital overlaps, but also must aim to reduce unfavorable molecular motions via unique  $\pi$ -core structures and effective side-chain engineering.

To meet all the aforementioned requirements for promising next-generation OSCs, our group has proposed a series of conceptually new bent-shaped  $\pi$ -cores.<sup>68–73</sup> The traditional linear and quasi-linear molecules have small radii of rotation and translation, which lead to low thermal durability as a result of constant molecular motions. In contrast, bent-shaped molecular geometries possess increased radii of rotation and translation, which suppress detrimental molecular motions in the solid state and simultaneously confer high  $\mu$  and thermal durability (Figure 2).<sup>74</sup> Another feature of the bent-shaped geometry compared to conventional linear and quasi-linear geometries is an enhanced internal dipole moment resulting from reduced molecular symmetry. On this basis, we attempted to develop highly soluble  $\pi$ -cores that can be solution-processed to fabricate OFETs and that permit fine-tuning of molecular packing structures with further side-chain engineering. Our group has thus far synthesized a series of bent-shaped molecules, including first- and second-generation OSCs, as well as extended analogues. Sulfur atoms were incorporated into these compounds to allow tuning of the electronic structures (specifically, the highest occupied molecular orbital (HOMO) energy level) to achieve efficient hole injections during OFET operations under ambient conditions. In addition, the large HOMO coefficient of the sulfur atom produces favorable intermolecular short-range interactions with adjacent  $\pi$ -cores. These lead to large intermolecular orbital overlaps (increased transfer integral ( $t$ ) values) and also suppress molecular motions in the solid state.

Herein, we summarize our recent work regarding the molecular design of bent-shaped OSCs by providing a detailed analysis of the synthesis, aggregated structures (complemented by theoretical calculations), ionization potentials, thermal stabilities, and solubilities of these compounds. The OFET performances of these bent-shaped OSCs are also presented to demonstrate the effectiveness of the molecular designs. We

## 1<sup>st</sup> Generation Bent-Shaped $\pi$ -Electron Cores

### “Molecular Shape” Engineering



## 2<sup>nd</sup> Generation Bent-Shaped $\pi$ -Electron Cores

### + “Molecular Orbital” Engineering

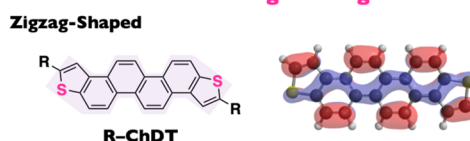
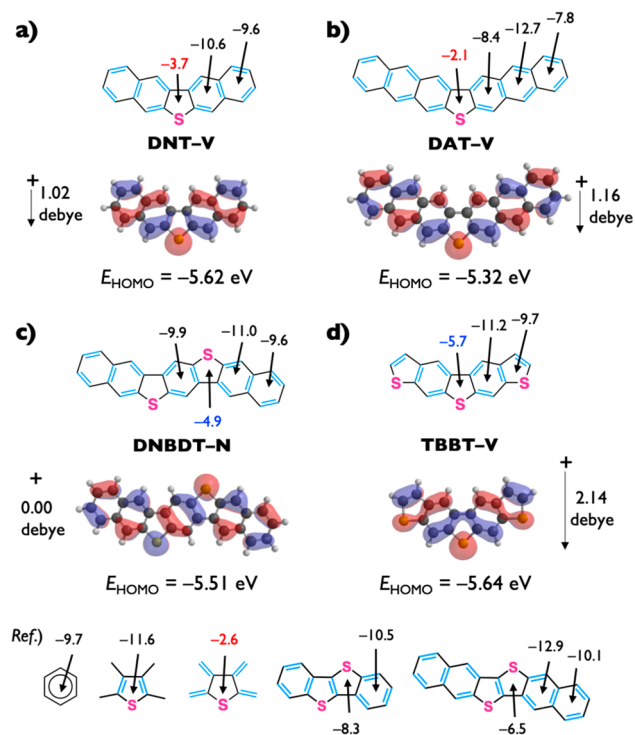


Figure 2. Molecular designs of first- and second-generation bent-shaped OSCs.

hope that this work will assist future molecular design of OSCs toward the development of high-performance next-generation electronics materials.

## ■ MOLECULAR DESIGN

**First-Generation OSCs Based on V- and N-Shaped  $\pi$ -Cores.** **DNT-V.** The V-shaped dinaphtho[2,3-*b*:2',3'-*d*]-thiophene (DNT-V)  $\pi$ -core was developed for *p*-channel OFET applications.<sup>68</sup> DNT-V features a thiophene in the center position that is fused by two naphthalene units on each side. The V-shaped molecular geometry and reduced molecular symmetry of this molecule produce an internal dipole moment that is not present in linear molecules, along with a stabilized crystalline phase (which suppresses molecular motions) and high solubility<sup>75</sup> in common organic solvents. Density functional theory (DFT) calculations revealed a delocalized distribution of HOMO coefficients across the backbone and a large HOMO coefficient of the sulfur atom (Figure 3a). The HOMO level of DNT-V was calculated to be  $-5.62 \text{ eV}$ , which is higher than that of BTBT ( $-5.79 \text{ eV}$ )<sup>42</sup> at the B3LYP/6-311G(d) level. In terms of reorganization energies for hole transport ( $\lambda_h$ ), our calculations estimate a  $\lambda_h$  of 138 meV for DNT-V, which is significantly smaller than that for BTBT (226 meV) and almost equal to that of DNNT (130 meV).<sup>76</sup> The large HOMO coefficient for the sulfur atom suggests that the central sulfur-based heterocycle is different from thiophene. From the nucleus-independent chemical shift (NICS),<sup>77,78</sup> we hope to gain fundamental understanding on the molecular properties of such fused heterocyclic systems, as well as predict their molecular assemblies and charge transports. Indeed, NICS calculations showed that the central ring is more similar to the less aromatic compound 2,3,4,5-tetramethylene-tetrahydrothiophene (thiophenoradialene)<sup>79</sup> (NICS(0) =  $-2.6 \text{ ppm}$ ) than to 2,3,4,5-tetramethylthiophene (NICS(0) =  $-11.6 \text{ ppm}$ ). Owing to this molecular feature, the large HOMO coefficient for sulfur can potentially contribute to significant intermolecular orbital overlaps that promote hole transports.



**Figure 3.** Molecular structures, NICS values (calculated at the HF/6-31+G(d)//B3LYP/6-31G(d) level), HOMO coefficients and energy levels, and dipole moments (calculated at the B3LYP/6-311G(d)//B3LYP/6-31G(d) level) of the (a) DNT-V, (b) DAT-V, (c) DNBDT-N, and (d) TBBT-V OSCs.

**DAT-V.** The recent molecular design of dianthra[2,3-*b*:2',3']thiophene (DAT-V)<sup>71</sup> (Figure 3b) involves the expansion of  $\pi$ -conjugation from the dinaphthalene moiety of DNT-V to a dianthracene group while preserving the overall V-shaped geometry. DFT calculations demonstrate a highly delocalized distribution of HOMO coefficients across the backbone and a sizable HOMO coefficient for the sulfur atom that is similar to that of DNT-V. Extending the  $\pi$ -conjugation increases the calculated HOMO energy level of DAT-V to -5.32 eV, compared to -5.62 eV for DNT-V, which is expected to lower the injection barrier and threshold voltage in OFET operation. NICS calculations showed that the central sulfur-based heterocycle exhibits a much lower degree of aromaticity (NICS(0) = -2.1 ppm). Another attractive feature of the DAT-V  $\pi$ -core is the reduced  $\lambda_{\text{h}}$  value (99 meV), which is significantly smaller than those for DNT-V (138 meV) and DNTT (130 meV).<sup>76</sup>

**DNBDT-N.** The N-shaped (dinaphtho[2,3-*d*:2',3'-*d'*]benzo[1,2-*b*:4,5-*b'*]dithiophene (DNBDT-N)<sup>70</sup>  $\pi$ -core (Figure 3c) is also considered as an extended V-shaped DNT-V  $\pi$ -core. DNBDT-N adopts a bent-shaped molecular geometry at two terminals that further suppresses molecular motions and stabilizes the crystal phase. The HOMO distribution of DNBDT-N is spread across the entire  $\pi$ -core, including a large coefficient of sulfur atoms. This scenario results in effective intermolecular orbital overlaps. The HOMO level calculated for DNBDT-N is -5.51 eV. This value is significantly higher than that for DNT-V and is attributed to the extended  $\pi$ -electron system of DNBDT-N. NICS calculations showed that the two heterocycle rings exhibit aromatic characteristics intermediate between those of thiophene and thiophenoradialene (NICS(0) = -4.9 ppm).

In addition, the increased molecular weight of DNBDT-N compared to the smaller DNT-V molecule would also impart improved thermal durability to thin-film devices.

**TBBT-V.** The V-shaped thieno[3,2-*f*:4,5-*f'*]bis[1]benzothiophene (TBBT-V) molecule (Figure 3d) has electronic and geometric characteristics similar to those of DNT-V, although the outer aromatic units are changed from benzene to thiophene rings. One of the obvious advantages associated with this modification is the ease of functionalizing the more reactive thiophene units, whereas the terminal benzene groups of the DNT-V  $\pi$ -core cannot be selectively functionalized. The HOMO level of the TBBT-V  $\pi$ -core was determined to be -5.64 eV, which is the same as that of DNT-V. However, the terminal thiophene units of the parent TBBT-V can be readily functionalized. As an example, the HOMO level of methyl-substituted TBBT-V (Me-TBBT-V) is increased to -5.50 eV, and further fine-tuning of the HOMO levels can be achieved depending on the choice of substitution. NICS calculations for TBBT-V revealed that the central heterocycle ring exhibits higher aromaticity than the other V- and N-shaped  $\pi$ -cores (NICS(0) = -5.7 ppm). With the incorporation of thiophene in TBBT-V, a high internal dipole moment of 2.14 D is obtained, indicating the potential for device fabrication based on solution processing.

**Second-Generation OSCs Based on W- and Zigzag-Shaped  $\pi$ -Cores.** DNT-W. The molecular design of W-shaped dinaphtho[1,2-*b*:2',1'-*d*]thiophene (DNT-W) (Figure 4) was

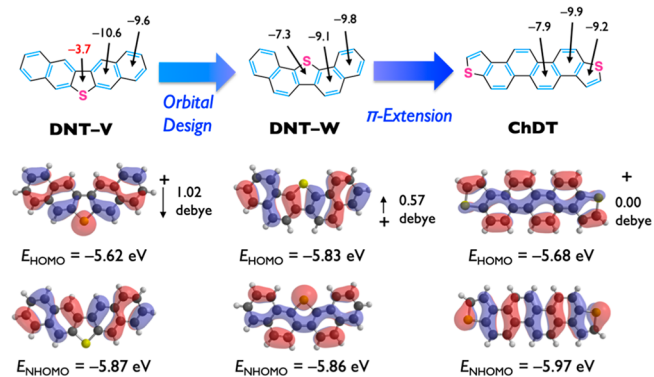


**Figure 4.** Molecular structures, NICS(0) values (calculated at the HF/6-31+G(d)//B3LYP/6-31G(d) level), HOMO and NHOMO coefficients and their energy levels, and dipole moments (calculated at the B3LYP/6-311G(d)//B3LYP/6-31G(d) level) of V-, W-, and zigzag-shaped  $\pi$ -cores.

inspired by the well-known picene backbone. Picene has been reported as a hole-transporting *p*-type OSC, although the performance of picene-based OFETs has been shown to be unstable under ambient conditions.<sup>80–82</sup> Moreover, the crystal structure of this compound suggests a relatively large displacement along the long axis, indicating the potential for significant variations in intermolecular orbital overlaps. Thus, we envisioned that a DNT-W  $\pi$ -core incorporating sulfur would provide effective and consistent intermolecular orbital overlaps as well as suppressed molecular motions. In fact, the HOMO and next HOMO (NHOMO) coefficients determined for DNT-W ( $E_{\text{HOMO}}$  = -5.83 eV,  $E_{\text{NHOMO}}$  = -5.86 eV) were determined to be almost degenerate. The calculation results show delocalized distributions of the HOMO and NHOMO and also a unique continuous NHOMO having a single phase over the entire  $\pi$ -core. Furthermore, NICS calculations

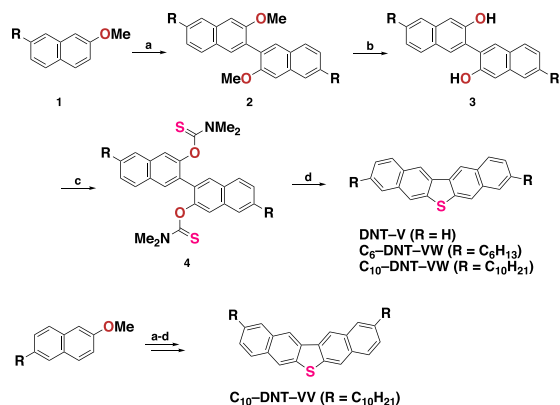
DNT-W determined that the central heterocycle ring has an almost aromatic character (NICS(0) =  $-7.3$  ppm). These unique characteristics of DNT-W suggest that it will provide the required degree of orbital overlap and also give a well-anchored molecular assembly, leading to high  $\mu$ .

**ChDT.** Our most recent zigzag-shaped  $\pi$ -core, chryseno[2,1-*b*:8,7-*b'*]dithiophene (ChDT), can be considered to be an extended version of DNT-W (Figure 4). In the case of ChDT, HOMO coefficients indicating the same phase ( $E_{\text{HOMO}} = -5.68$  eV) extend across the entire  $\pi$ -core, including the terminal thiophene sulfur atoms, which is the same as the NHOMO in DNT-W. NICS calculations for ChDT showed that the terminal heterocycle ring and other aromatic rings have the same aromatic character as benzene (NICS(0) =  $-9.2$  ppm). The incorporation of two terminal thiophene units lowered the HOMO energy levels of ChDT derivatives, which is expected to promote hole injection and provide lower threshold voltages. These terminal thiophene groups also allow facile derivatizations due to the highly reactive  $\alpha$ -positions.

## SYNTHESIS

The synthetic route to DNT-V and its derivatives is illustrated in Scheme 1. Previously, the synthesis of a similar sulfur-

### Scheme 1. Synthesis of DNT-V Derivatives<sup>a</sup>

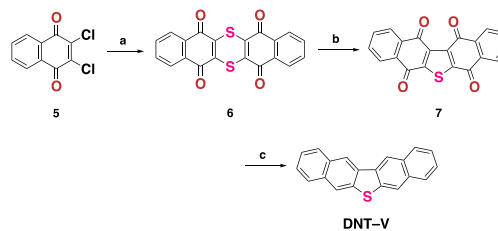


<sup>a</sup>Reagents and conditions: (a) *n*-BuLi, Fe(acac)<sub>3</sub>, 0 °C to rt, 73% (R = C<sub>10</sub>H<sub>21</sub>); (b) BBr<sub>3</sub>, 0 °C to rt, 94% (R = H), 97% (R = C<sub>10</sub>H<sub>21</sub>); (c) dimethylcarbamyl chloride, Et<sub>3</sub>N, pyridine, THF, 65 °C, 78% (R = H), 75% (R = C<sub>10</sub>H<sub>21</sub>); (d) 300–320 °C, 81% (R = H), 77% (R = C<sub>10</sub>H<sub>21</sub>).

bridged  $\pi$ -core was reported via a 10-step process, but gave only a 12% total yield.<sup>83</sup> In the present work, we developed a facile four-step synthesis to obtain the target compounds using the readily available compound **1** as a starting material. The first step features a selective *ortho*-lithiation with *n*-BuLi followed by a Fe(acac)<sub>3</sub>-catalyzed oxidative homocoupling to afford the dimerized **2** in good yield. After a demethylation reaction using BBr<sub>3</sub>, the sulfur atom is installed on the naphthalene dimer using thiocarbamoyl, followed by a solventless annulation via Newman–Kwart rearrangement<sup>84</sup> at 320 °C, to generate the target compound DNT-V in 42% total yield over four steps. Various alkyl-substituted DNT-V derivatives can be obtained by means of the same synthetic route using alkylated versions of **1** as starting materials.

Recently, our group developed a simple alternative synthetic route that provides the DNT-V core in only three steps (Scheme 2). This process employs a modification of a

### Scheme 2. Modified DNT-V Synthesis<sup>a</sup>

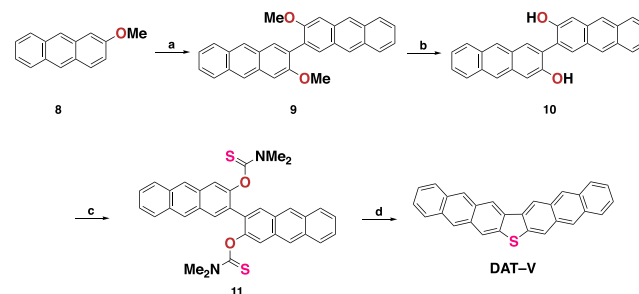


<sup>a</sup>Reagents and conditions: (a) (1) dithioamide, DMF, 55 °C, (2) Et<sub>3</sub>N, rt, 89%; (b) *m*-CPBA, CH<sub>2</sub>Cl<sub>2</sub>, 30 °C, 88%; (c) HI, AcOH, reflux, 97%.

previously reported strategy using compound **5** as the starting material to afford the key precursor **6** in excellent yield.<sup>85</sup> A subsequent reduction of the tetraone compound **7** with aqueous hydroiodic acid in acetic acid affords DNT-V in 97% yield, with a total yield of 77% over three steps. Thus, this represents an improvement compared to our previous route. Our current synthetic scheme also avoids the high-temperature Newman–Kwart rearrangement featured in the previous strategy. In addition, expensive transition metal catalysts such as palladium are not required, and the synthesis is well-suited to large-scale production.

Although a synthesis of DAT-V was previously reported,<sup>86</sup> we synthesized DAT-V via a process similar to that used to obtain DNT-V (Scheme 3). We employed the anthracene-

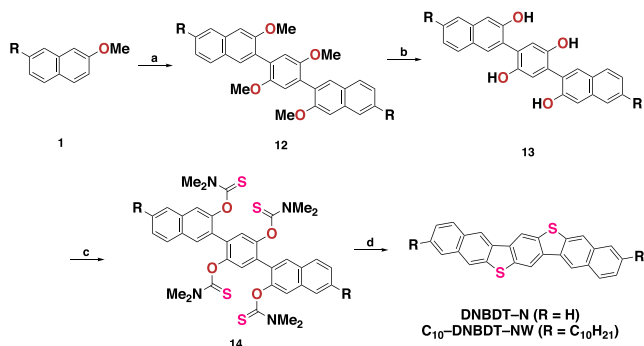
### Scheme 3. Synthesis of DAT-V<sup>a</sup>



<sup>a</sup>Reagents and conditions: (a) *n*-BuLi, Fe(acac)<sub>3</sub>, 0 °C to rt, 52%; (b) BBr<sub>3</sub>, 0 °C to rt, 96%; (c) dimethylcarbamyl chloride, Et<sub>3</sub>N, pyridine, THF, 65 °C, 61%; (d) 300 °C, 68%.

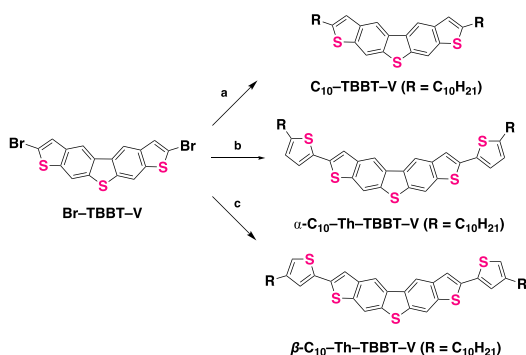
based precursor **8** as the starting material and conducted a Fe(acac)<sub>3</sub>-catalyzed homocoupling to afford the dimer, followed by a demethylation with BBr<sub>3</sub> to give compound **10** in excellent yield. From **11**, we carried out a Newman–Kwart rearrangement to generate DAT-V in satisfactory yield.

DNBDT-N and decyl-substituted DNBDT-NW (C<sub>10</sub>-DNBDT-NW) were synthesized in a manner similar to that used for DNT-V and its derivatives (Scheme 4). From **1**, selective lithiation with *n*-BuLi followed by transmetalation afforded the arylzinc intermediate, which was further reacted with 1,4-dibromo-2,5-dimethoxybenzene via Negishi cross-coupling to provide **12** in good yield. Subsequently, demethylation with BBr<sub>3</sub> generated the tetra-hydroxyl intermediate **13** with subsequent installation of thiocarbamate groups. The target DNBDT-N derivatives were realized by the Newman–Kwart rearrangement under solventless conditions in 64–67% yield.

Scheme 4. Synthesis of DNBDT-N Derivatives<sup>a</sup>

<sup>a</sup>Reagents and conditions: (a) (1) *n*-BuLi, ZnCl<sub>2</sub>, 0 °C to rt, (2) 1,4-dibromo-2,5-dimethoxybenzene, PdCl<sub>2</sub>(dppp), 50 °C, 87% (R = H), 85% (R = C<sub>10</sub>H<sub>21</sub>); (b) BBr<sub>3</sub>, 0 °C to rt, 81% (R = H), 92% (R = C<sub>10</sub>H<sub>21</sub>); (c) dimethylcarbamyl chloride, Et<sub>3</sub>N, pyridine, THF, 65 °C, 53% (R = H), 72% (R = C<sub>10</sub>H<sub>21</sub>); (d) 310–320 °C, 67% (R = H), 64% (R = C<sub>10</sub>H<sub>21</sub>).

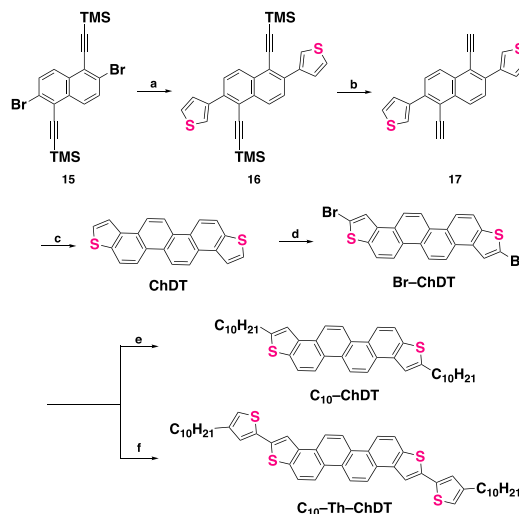
The **TBBT-V**  $\pi$ -core was synthesized according to a procedure previously reported in the literature.<sup>87</sup> This parent  $\pi$ -core was then used to produce three derivatives: **C<sub>10</sub>-TBBT-V**,  **$\alpha$ -C<sub>10</sub>-Th-TBBT-V**, and  **$\beta$ -C<sub>10</sub>-Th-TBBT-V** (Scheme 5).

Scheme 5. Synthesis of TBBT-V Derivatives<sup>a</sup>

<sup>a</sup>Reagents and conditions: (a) C<sub>10</sub>H<sub>21</sub>ZnCl<sub>2</sub>, PdCl<sub>2</sub>(dppf)·CH<sub>2</sub>Cl<sub>2</sub>, toluene, 70 °C, 64%; (b) (5-decylthiophen-2-yl)trimethylstannane, Pd(PPh<sub>3</sub>)<sub>4</sub>, LiCl, DMF, 100 °C, 86%; (c) (4-decylthiophen-2-yl)trimethylstannane, Pd(PPh<sub>3</sub>)<sub>4</sub>, LiCl, DMF, 100 °C, 92%.

**TBBT-V** was brominated by sequential treatment with lithium 2,2,6,6-tetramethylpiperidide (to deprotonate the  $\alpha$ -positions of the thiophene) and 1,2-dibromo-1,1,2,2-tetrachloroethane, to afford **Br-TBBT-V**. **C<sub>10</sub>-TBBT-V** was synthesized in 64% yield, whereas  **$\alpha$ -C<sub>10</sub>-Th-TBBT-V** and  **$\beta$ -C<sub>10</sub>-Th-TBBT-V** were furnished in 86% and 92% yields, respectively. The facile reactions at the  $\alpha$ -positions demonstrate the ease of functionalization of **TBBT-V** and the ready tuning of its molecular properties.

**DNT-W** was furnished in a one-pot reaction according to a previously reported procedure.<sup>88</sup> The synthesis of **ChDT** (Scheme 6) started from compound **15**, which was readily synthesized according to a literature procedure.<sup>89</sup> From **15**, a halogen–lithium exchange and a transmetalation with zinc chloride were performed, followed by a Negishi cross-coupling to install the thiophene moieties, giving an overall yield of 79%. Facile removal of the trimethylsilyl protecting groups was carried out under basic conditions to give compound **17** in

Scheme 6. Synthesis of ChDT Derivatives<sup>a</sup>

<sup>a</sup>Reagents and conditions: (a) (1) *n*-BuLi, THF, –78 °C, (2) ZnCl<sub>2</sub>, THF, 0 °C, (3) 3-bromothiophene, Pd<sub>2</sub>(dba)<sub>3</sub>·CHCl<sub>3</sub>, THF, 50 °C, 79%; (b) K<sub>2</sub>CO<sub>3</sub>, MeOH, CH<sub>2</sub>Cl<sub>2</sub>, rt, 99%; (c) PtCl<sub>2</sub>, DMF, 80 °C, 58%; (d) (1) LiTMP, THF, –78 °C to –50 °C, (2) 1,2-dibromo-1,1,2,2-tetrachloroethane, –78 °C to rt, 88%; (e) C<sub>10</sub>H<sub>21</sub>ZnCl, PdCl<sub>2</sub>(dppf)·CH<sub>2</sub>Cl<sub>2</sub>, THF, 70 °C, 80%; (f) (4-decylthiophen-2-yl)trimethylstannane, Pd(PPh<sub>3</sub>)<sub>4</sub>, LiCl, DMF, 100 °C, 81%.

excellent yield. Subsequently, we used PtCl<sub>2</sub> to catalyze the 6-*exo-dig* double cyclizations in DMF to furnish the **ChDT**  $\pi$ -core in satisfactory yield.<sup>90</sup> The  $\alpha$ -positions of the thiophene were readily brominated by sequential treatments with lithium tetramethylpiperidide and 1,1,2,2-tetrachloro-1,2-dibromoethane to afford the key precursor **Br-ChDT** in 88% yield. Two **ChDT** derivatives, **C<sub>10</sub>-ChDT** and **C<sub>10</sub>-Th-ChDT**, were prepared using Negishi and Stille cross-coupling reactions, respectively, in excellent yields.

## ■ AGGREGATED STRUCTURES, THEORETICAL CALCULATIONS, THERMAL STABILITIES, IONIZATION POTENTIALS, AND SOLUBILITIES

### Aggregated Structures and Theoretical Calculations.

To understand the aggregated structures and charge-carrier transports of the current bent-shaped OSCs, we examined single crystals of the bent-shaped parent  $\pi$ -cores and their derivatives, grown by either physical vapor transport (PVT)<sup>91,92</sup> or solution techniques, using X-ray diffraction (XRD). A common feature observed in single crystals of V-shaped OSCs was their slightly bent geometries (Figure 5 and

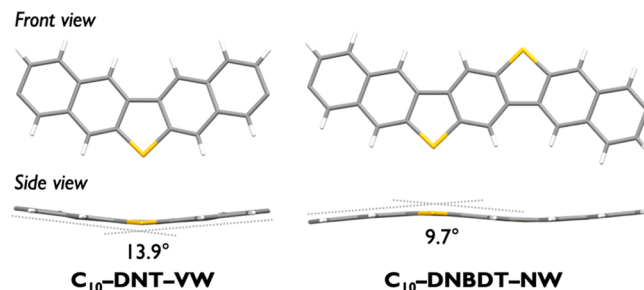
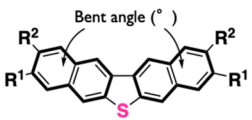


Figure 5. Representative slightly bent geometries of **C<sub>10</sub>-DNT-VW** and **C<sub>10</sub>-DNBDT-NW** (front and side views) in single crystals.

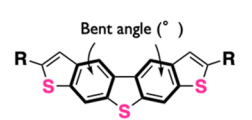
Table 1), which differ from the planar conformations suggested by DFT studies. The bent angles increased when substituents

**Table 1. Packing Modes and Twist Angles for V-, N-, and W-Shaped Derivatives**



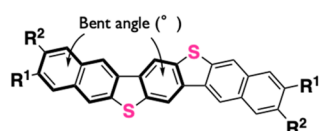
**DNT-Vs**

**DNT-V** ( $R^1 = R^2 = H$ )  
**C<sub>10</sub>-DNT-VW** ( $R^1 = C_{10}H_{21}, R^2 = H$ )  
**C<sub>10</sub>-DNT-VV** ( $R^1 = H, R^2 = C_{10}H_{21}$ )



**TBBT-Vs**

**TBBT-V** ( $R = H$ )  
**C<sub>10</sub>-TBBT-V** ( $R = C_{10}H_{21}$ )



**DNBDT-Ns**

**DNBDT-N** ( $R^1 = R^2 = H$ )  
**C<sub>10</sub>-DNBDT-NW** ( $R^1 = C_{10}H_{21}, R^2 = H$ )

compound	packing mode	bent angle (deg)
DNT-V	HB	13.9
C <sub>10</sub> -DNT-VW	HB	13.3
C <sub>10</sub> -DNT-VV	HB	18.0
DAT-V	HB	17.2
TBBT-V	HB	10.0
C <sub>10</sub> -TBBT-V	HB	11.3
DNBDT-N	$\pi$ - $\pi$ stacking ( $\pi$ - $\pi$ ), slipped HB	0.0
C <sub>10</sub> -DNBDT-NW	HB	9.7
DNT-W	HB	9.1

were added to the  $\pi$ -cores, as a result of increased attractive intermolecular interactions. N-shaped and second-generation zigzag-shaped OSCs were also observed. The bent geometry in these derivatives potentially allowed for C-H $\cdots$  $\pi$  and S $\cdots$  $\pi$  interactions between the prominent central sulfur atom and the adjacent backbone. As a result, higher degrees of intermolecular HOMO overlaps and greater suppression of molecular motions were realized, both of which improve charge-carrier transport and thermal durability.

The parent DNT-V, DAT-V, and TBBT-V  $\pi$ -cores were found to adopt 2D HB packing structures, whereas the DNBDT-N demonstrated a less attractive one-dimensional (1D)  $\pi$ - $\pi$  stacking motif that does not favor charge transport (Table 1). Following the incorporation of various substituents, the packing structures of the V-shaped OSCs were effectively modified to give high degrees of intermolecular orbital overlap, as indicated by the increased absolute  $t$  values (Table 2). As for the sign of  $t$ , the negative and positive intermolecular orbital overlaps result in positive and negative transfer integrals, respectively (Figure 6).

Both C<sub>10</sub>-DNT-VW and C<sub>6</sub>-DNT-VW had larger absolute  $t$  values than the DNT-V  $\pi$ -core, whereas C<sub>10</sub>-DNT-VV exhibited lower  $t$  values (Figure 7). Since C<sub>10</sub>- and C<sub>6</sub>-DNT-VW exhibit almost the same HOMO and NHOMO energy levels, the  $t$  values between these levels are estimated, and are listed in Table 2. The packing structures of the DNT-V series suggest that more effective intermolecular orbital overlaps were achieved by installing the alkyl chains in the VW fashion. As a

**Table 2. Summary of Transfer Integrals for V-Shaped Derivatives**

compound	packing mode and HB angle (deg) <sup>a</sup>	transfer integral, $t$ (meV) <sup>b</sup>		
		$t_{HT}$	$ t_{HH} $	$ t_{TT} $
DNT-V	HB, 45.8°	+37	46	13
C <sub>10</sub> -DNT-VW	HB, 45.3°	+18 <sup>c</sup>	14 <sup>c</sup>	32 <sup>c</sup>
		+45 <sup>d</sup>	61 <sup>d</sup>	37 <sup>d</sup>
C <sub>6</sub> -DNT-VW	HB, 46.4°	+44 <sup>c</sup>	63 <sup>c</sup>	36 <sup>c</sup>
		+19 <sup>d</sup>	10 <sup>d</sup>	17 <sup>d</sup>
C <sub>10</sub> -DNT-VV	HB, 36.0°	+35	42	15
DAT-V	HB, 38.9°	+41	20	6.4
C <sub>10</sub> -TBBT-V	HB, 43.6°	+52	67	10

<sup>a</sup>Herringbone (HB) angles between two mean planes of the  $\pi$ -cores were 56.4° (at 293 K),<sup>93</sup> 52.5° (at 293 K),<sup>43</sup> and 51.1° (at 200 K)<sup>52</sup> for C<sub>8</sub>-TBBT, DNNT, and C<sub>10</sub>-DNNT as references. <sup>b</sup>Transfer integrals were calculated at the PBEPBE/6-31G(d) level. <sup>c</sup>Transfer integrals between HOMOs. <sup>d</sup>Transfer integrals between NHOMOs.

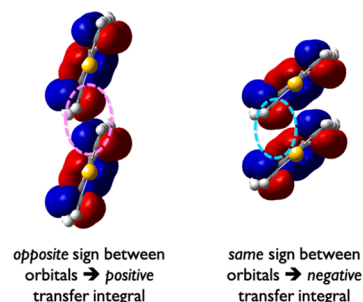


**Figure 6.** Relation between sign of transfer integral and intermolecular orbital overlap.

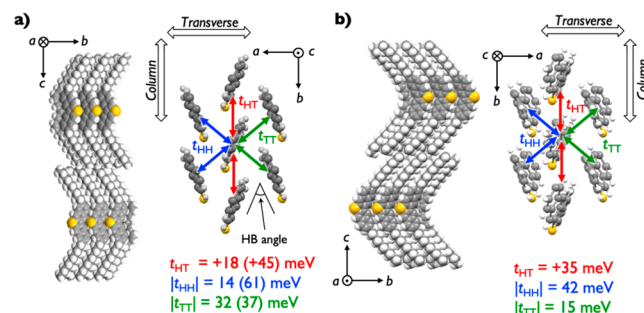


**Figure 7.** Representative packing structures and transfer integrals for (a) C<sub>10</sub>-DNT-VW and (b) C<sub>10</sub>-DNT-VV for their HOMOs (and NHOMO).

consequence, the charge transport capabilities were significantly affected by the alkyl chain positions. Owing to the intrinsic disorder of the  $\alpha$ -C<sub>10</sub>-Th-TBBT-V and  $\beta$ -C<sub>10</sub>-Th-TBBT-V, only C<sub>10</sub>-TBBT-V single crystals could be obtained from the TBBT-V series. The HB packing structure of the C<sub>10</sub>-TBBT-V showed a significantly larger  $t$  value in the head-to-tail ( $t_{HT}$ ) direction than in the head-to-head ( $t_{HH}$ ) and tail-to-tail ( $t_{TT}$ ) directions, suggesting anisotropic 2D charge-transport properties.

Different from the 1D  $\pi$ - $\pi$  stacking structure of DNBDT-N, C<sub>10</sub>-DNBDT-NW formed an HB motif with a layer-by-layer structure (Figure 8). The 2D cofacial molecular arrangement through strong  $\pi$ - $\pi$  and C-H $\cdots$  $\pi$  interactions resulted in equal  $t$  in the column and transverse directions ( $t_c = +52$  meV,  $t_t =$

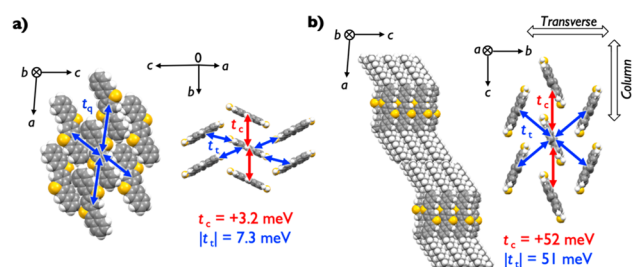


**Figure 8.** Representative packing structures and transfer integrals for (a) DNBDT-N and (b) C<sub>10</sub>-DNBDT-NW.

+51 meV), demonstrating favorable 2D charge-transport properties (Table 3).

**Table 3. Summary of Transfer Integrals for N-Shaped Derivatives**

compound	packing mode and HB angle (deg) <sup>a</sup>	transfer integral, $t$ (meV) <sup>b</sup>	
		$t_{\text{column}}$ ( $t_c$ )	$ t_{\text{trans}} $ ( $ t_t $ )
DNBDT-N	$\pi$ - $\pi$ and slipped HB, 126.5°	+3.2	7.3
C <sub>10</sub> -DNBDT-NW	HB, 46.7°	+52	51

<sup>a</sup>Herringbone (HB) angles between two mean planes of the  $\pi$ -cores.

<sup>b</sup>Transfer integrals were calculated at the PBEPBE/6-31Gd level.

The second-generation zigzag-shaped OSCs all exhibited HB packing structures in the crystalline state (Table 4). DNT-W showed reasonable positive  $t$  values in the head-to-tail ( $t_{\text{HT}}$ ) and tail-to-tail ( $t_{\text{TT}}$ ) directions, but larger absolute  $t$  values in the transverse head-to-head ( $t_{\text{HH}}$ ) direction (Figure 9). The ChDT derivatives showed strong intermolecular C–H $\cdots$  $\pi$  and S $\cdots$  $\pi$  interactions in the HB motif. The parent ChDT demonstrated large absolute  $t$  values in both the column ( $t_c$ ) and transverse ( $t_t$ ) directions, but adding C<sub>10</sub>-alkyl chains on both sides dramatically lowered the absolute  $t$  value in the transverse direction. Consequently, the C<sub>10</sub>-ChDT shows 1D charge transport. Although the  $t_c$  and  $t_t$  values for C<sub>10</sub>-Th-ChDT are well-balanced, these values are relatively small compared to other ChDT derivatives. Thus, the primary reason for the smaller absolute  $t$  values for C<sub>10</sub>-Th-ChDT is the much longer  $\pi$ - $\pi$  stacking distance (6.90 Å) compared to ChDT (5.97 Å), due to the steric hindrance of the decylthienyl groups.

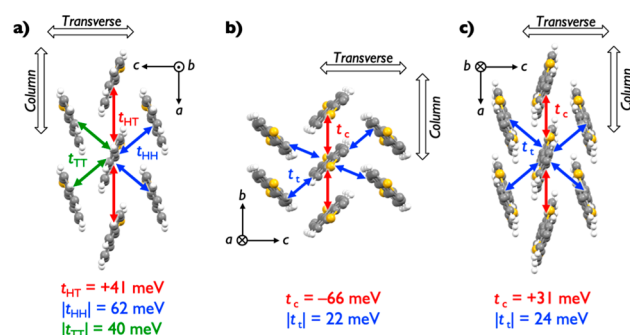
**Table 4. Summary of (Top) Transfer Integrals of DNT-W and (Bottom) Transfer Integrals, Lattice Constants in the Column Direction, and Effective Masses for C<sub>10</sub>-ChDT, C<sub>10</sub>-Th-ChDT, and C<sub>10</sub>-DNBDT-NW**

compound	packing mode and HB angle (deg) <sup>a</sup>	transfer integral, $t$ (meV) <sup>a</sup>		
		$t_{\text{HT}}$	$ t_{\text{HH}} $	$ t_{\text{TT}} $
DNT-W	HB, 41.6°	+41	62	40

compound	packing mode and HB angle (deg) <sup>a</sup>	transfer integral, $t$ (meV) <sup>b</sup>		lattice constant in the column direction, $d_c$ (Å)	effective mass, $^c m_{\parallel}^*/m_0$ , $^d m_{\perp}^*/m_0$
		$t_{\text{column}}$ ( $t_c$ )	$ t_{\text{trans}} $ ( $ t_t $ )		
C <sub>10</sub> -ChDT	HB, 89.2°	−66	22	4.861	2.55, 17.2
C <sub>10</sub> -Th-ChDT	HB, 39.2°	+31	24	6.899	1.86, 5.85
C <sub>10</sub> -DNBDT-NW	HB, 46.7°	+52	51	6.127	1.31, 2.52

<sup>a</sup>Herringbone (HB) angles between two mean planes of the  $\pi$ -core. <sup>b</sup> $t$  values were calculated at the PBEPBE/6-31G(d) level. <sup>c</sup> $m_0$  is the electron rest mass. <sup>d</sup> $m^*$  in the column direction. <sup>e</sup> $m^*$  in the transverse direction.



**Figure 9.** Representative packing structures and transfer integrals for (a) DNT-W, (b) C<sub>10</sub>-ChDT, and (c) C<sub>10</sub>-Th-ChDT.

Experimental studies have revealed that OSCs having high  $\mu$  show band transport characteristics,<sup>59,70,74,94,95</sup> with delocalized wave-like carriers over multiple molecules. Based on the band theory, the mobility  $\mu$  of carrier with charge  $q$  is inversely proportional to the effective mass ( $m^*$ ) according to the following equation:

$$\mu = q \frac{\tau}{m^*}$$

where  $\tau$  is the relaxation time. HOMO band structures,  $E(k)$ , are obtained by the tight-binding approximation using  $t$  values. Effective masses of holes are calculated as the following equation along the respective directions:

$$\frac{1}{m^*} = \frac{1}{\hbar^2} \frac{d^2 E}{dk^2}$$

In the case of the HB-type packing structure studied herein, the top of the HOMO band is located on the  $\Gamma$  ( $k = 0$ ) point, and the column direction exhibits the highest mobility, except for C<sub>10</sub>-ChDT. Therefore, we investigate  $1/m^*$  at the  $\Gamma$  point along the column direction, given by the following equation:

$$\frac{1}{m^*} = \frac{1}{\hbar^2} d^2 (2t_{\text{column}} + |t_{\text{trans}}|)$$

Here,  $t_{\text{column}}$  ( $t_c$  or  $t_{\text{HT}}$ ) and  $t_{\text{trans}}$  ( $t_t$  or  $t_{\text{HH}}$ ,  $t_{\text{TT}}$ ) (see Figures 7–9) refer to the transfer integrals in the column (H-to-T) and transverse (H-to-H and T-to-T) directions of HB packing motif, respectively, and  $d$  refers to the lattice constant in the column direction. That is, the reciprocal of the effective mass is proportional to the transfer integral and the square of the

lattice constant. In particular,  $t_c$  is twice as effective as  $t_b$ , and its sign (whether they are either positive or negative) is also important, as described in Figure 6.

Notably, the effective mass in the column and transverse directions ( $m_{\parallel}^*$  and  $m_{\perp}^*$ ) for  $C_{10}$ -Th-ChDT (1.86  $m_0$  and 5.85  $m_0$ ) was found to be much smaller and more isotropic than for  $C_{10}$ -ChDT ( $m_{\parallel}^* = 2.55 m_0$  and 17.2  $m_0$ ) and nearly comparable to that of  $C_{10}$ -DNBDT-NW ( $m_{\parallel}^* = 1.31 m_0$  and 2.52  $m_0$ ) (see Figure 10). These data indicate that increasing

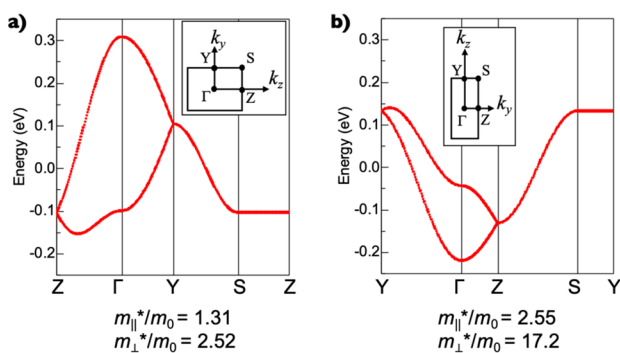


**Figure 10.** HOMO band structures and effective masses of (a)  $C_{10}$ -DNBDT-NW and (b)  $C_{10}$ -ChDT. The origin of energy axis is set to HOMO level of the molecule. Insets show the first Brillouin zone with symmetry points of  $\Gamma(0,0,0)$ ,  $Y(0,\pi/b,0)$ ,  $Z(0,0,\pi/c)$ , and  $S(0,\pi/b,\pi/c)$ , where  $b$  and  $c$  are the lattice constants shown in Figures 8b and 9b. The column directions correspond to  $\Gamma$ -Z ( $C_{10}$ -DNBDT-NW) and  $\Gamma$ -Y ( $C_{10}$ -ChDT) directions in the reciprocal lattice.

the lattice constant of  $C_{10}$ -Th-ChDT in the column direction compensates for the reduction of the transfer integral, resulting in a small effective mass.

Motivated by the intriguing HOMO configuration of ChDT, we investigated the variance in  $t$  ( $\Delta t$ ) values. It should be noted that the out-of-plane motion was the most prominent direction of molecular vibrations in the HB packing (Figure 11).<sup>67</sup> A smaller  $\Delta t$  of 5 meV was determined for ChDT, compared to those for DNNT (13 meV) and pentacene (29 meV) over the range of 0.13–0.18 Å. The small  $\Delta t$  for ChDT is a good indication of consistent intermolecular orbital overlaps in the solid state.

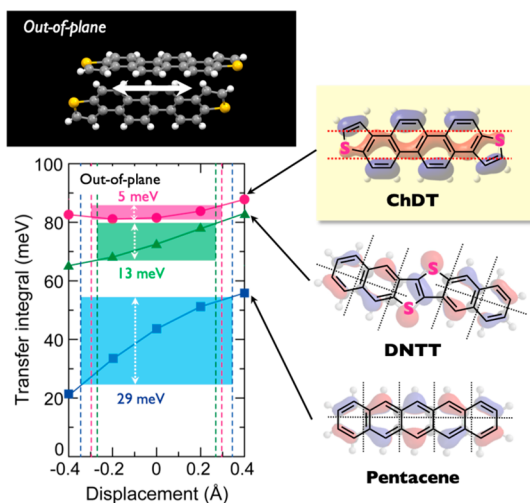


**Figure 11.** Values of  $t$  and  $\Delta t$  for ChDT, DNNT, and pentacene.

**Thermal Stability.** One crucial benefit of the bent-shaped molecular design is the prevention of phase transitions at low temperatures by the suppression of molecular motions. Analysis of the DNT-V derivatives by thermogravimetry (TG) did not show any thermal decomposition before 500 °C. Differential scanning calorimetry (DSC) studies also demonstrated high phase transition temperatures of 202 and 151 °C for  $C_6$ - and  $C_{10}$ -DNT-VW, respectively, but a value of only 90 °C in the case of  $C_{10}$ -DNT-VV. This lower temperature is attributed to the large displacements between adjacent molecules in the crystal packing structure of this compound, which result in reduced structural stability. The  $C_{10}$ -DNBDT-NW showed higher phase transition and decomposition temperatures than the V-shaped  $C_{10}$ -DNT-VW, resulting from the multiple intermolecular interactions and higher molecular weight of the former.  $C_{10}$ -DNBDT-NW in a thin film device demonstrated no phase transition up to 200 °C. More importantly,  $C_{10}$ -DNBDT-NW is a double V-shaped molecule, and thus should exhibit more effective suppression of molecular motions and stabilization of the crystalline phase compared to the DNT-V series. Both  $C_{10}$ -TBBT-V and  $\beta$ - $C_{10}$ -Th-TBBT-V showed multiple phase transition peaks during differential thermal analyses, potentially due to their lower structural rigidity and intrinsic disordering. In contrast,  $\alpha$ - $C_{10}$ -Th-TBBT-V showed a phase transition peak above 200 °C. The zigzag-shaped  $C_{10}$ -ChDT and  $C_{10}$ -Th-ChDT exhibited no phase transitions until above 250 °C. The excellent thermal stability of the current bent-shaped OSCs confirm their physical and chemical robustness, which would permit common purification techniques such as sublimation and PVT. These materials would also be expected to be thermally durable in the solid state.

**Ionization Potentials.** The electronic properties of these OSCs were further examined using photoelectron yield spectroscopy (PYS) to evaluate the ionization potential (IP) values. The resulting IP values were generally in good agreement with the HOMO energy levels calculated based on DFT. The DNT-V  $\pi$ -core was found to have a somewhat high IP of 5.72 eV, while extending the  $\pi$ -conjugation gave a considerably smaller IP of 5.21 eV for DAT-V. TBBT-V demonstrated an IP of 5.61 eV, similar to that for DNT-V. However,  $C_{10}$ -TBBT-V,  $\alpha$ - $C_{10}$ -Th-TBBT-V, and  $\beta$ - $C_{10}$ -Th-TBBT-V demonstrated effective tuning of the IP due to the synthetic versatility of the TBBT-V  $\pi$ -core, with values of 5.26, 5.10, and 5.01 eV, respectively. The IP value for the extended N-shaped  $C_{10}$ -DNBDT-NW was 5.24 eV, which also indicates an improvement relative to the DNT-V series. The zigzag-shaped DNT-W showed a large IP of 5.87 eV as a result of its relatively short  $\pi$ -conjugation, while the extended analogues  $C_{10}$ -ChDT and  $C_{10}$ -Th-ChDT had values of 5.56 and 5.53 eV, respectively. Overall, these data confirm fine-tuning of the IP values of the current bent-shaped OSCs by modifying the  $\pi$ -conjugation length and varying the functional groups. Such modifications achieved air-stable  $p$ -type performance, and also would be expected to reduce the injection barrier and threshold voltage associated with OFET operations.

**Solubility.** In contrast to the poor solubility of unsubstituted linear and quasi-linear  $\pi$ -cores (e.g., <0.001 wt% in toluene for DNNT), DNT-V demonstrated superior solubility of up to 0.30 wt% in common organic solvents such as chloroform and toluene at room temperature. Alkyl-substituted DNT-V derivatives showed improved solubility, ranging from 0.38 to 1.53 wt% in the case of the DNT-VW series. In



addition, extremely high solubilities in the range of 9.23–15.6 wt% were achieved with the DNT-VV derivative. The unsubstituted TBBT-V showed high solubility on the order of 0.1 wt% due to its large internal dipole moment, while C<sub>10</sub>-TBBT-V possessed the highest solubility of up to 1.1 wt%. Owing to the increased  $\pi$ -conjugation and molecular weight of DNBDT-N, the parent  $\pi$ -core exhibited limited solubility. However, the incorporation of C<sub>10</sub>-alkyl chains resulted in adequate solubility for C<sub>10</sub>-DNBDT-NW of up to 0.043 wt% in common organic solvents at a slightly elevated temperature. Having an equally extended  $\pi$ -conjugated system, C<sub>10</sub>-ChDT and C<sub>10</sub>-Th-ChDT showed higher solubilities of 0.068 and 0.13 wt% in toluene, respectively, than C<sub>10</sub>-DNBDT-NW. The high solubility and thermally stable crystal phases of the bent-shaped OSCs suggest that they show promises with regard to applications in thin-film OFET fabrication via solution-processing methods.

**Summary of Properties.** The bent-shaped OSCs presented herein exhibit unique NICS values, which suggest that the fused sulfur-containing heterocycles behave more like thiophenradialene, rather than thiophene. The consequence of such behaviors is that the sulfur atom possesses protruding HOMO that are likely to reinforce the molecular assembly and charge transports. The aggregated structures of bent-shaped OSCs all exhibit some degree of nonplanarity, or bentness, which lead to enhancement of their intermolecular interactions in the favorable herringbone packing structures. Theoretical calculations of transfer integrals and effective masses suggest favorable charge transport properties that are promising for achieving high  $\mu$ . Thermal studies suggest that the bent-shaped OSCs are thermally stable, and their crystal phases are thermally durable for sustaining elevated-temperature fabrication processes. Compared to the conventional linear and quasi-linear OSCs, the bent-shaped OSCs have their unique advantages to achieve high-performance and robust OSCs for future practical applications.

## OFET PERFORMANCE

To evaluate the device performance of bent-shaped OSCs, single-crystalline-based bottom-gate/top-contact OFETs were fabricated using either manual lamination (ML) or the solution-processed edge-casting (EC) technique that our group previously developed<sup>48–51</sup> (Figure 12 and Supporting

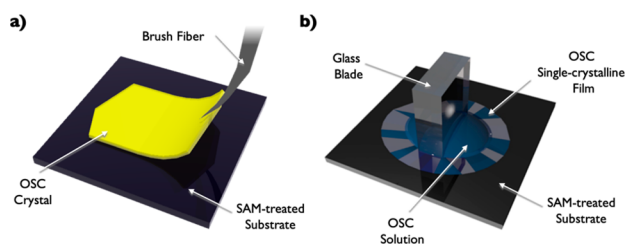


**Figure 12.** Schematic diagrams of (a) the manual lamination and (b) edge-casting techniques.

Information). These *p*-channel OFETs were produced by adding the strong electron acceptor F<sub>4</sub>-TCNQ between the OSC layer and the gold electrodes to reduce contact resistance. The transistors employed SiO<sub>2</sub>/Si substrates treated with heptadecafluorodecyltrimethoxysilane (F-DTS) in conjunction with the ML technique and either decyltrimethoxysilane (DTS) or  $\beta$ -phenylethyltrimethoxysilane ( $\beta$ -PTS) for the EC

technique. All devices incorporating bent-shaped derivatives demonstrated air-stable *p*-channel OFET characteristics.

The parent DNT-V single-crystalline thin-film OFET achieved a satisfactory  $\mu_h$  of 1.5 cm<sup>2</sup> V<sup>-1</sup> s<sup>-1</sup>, which is similar to the value obtained for a vacuum-deposited polycrystalline thin-film OFET (1.1 cm<sup>2</sup> V<sup>-1</sup> s<sup>-1</sup>). [All reported  $\mu$  values are summarized in Table 5.] The highest  $\mu_h$  of 9.5 cm<sup>2</sup> V<sup>-1</sup> s<sup>-1</sup> was

**Table 5. Characteristics of Field-Effect Transistors with Bent-Shape  $\pi$ -Cores**

compound	process, <sup>a</sup> SAM, and SiO <sub>2</sub> thickness (nm)	$\mu_{\max}$ (cm <sup>2</sup> /(V·s))	$\mu_{\text{avg}}$ (cm <sup>2</sup> /(V·s)) <sup>b</sup>
DNT-V	VD, <sup>c</sup> DTS, 500	1.1	0.91
DNT-V	ML, F-DTS, 500	1.5	1.0
C <sub>6</sub> -DNT-VW	VD, <sup>d</sup> DTS, 500	3.7	3.6
C <sub>6</sub> -DNT-VW	EC, $\beta$ -PTS, 500	9.5	6.2
C <sub>10</sub> -DNT-VV	VD, <sup>d</sup> DTS, 500	0.45	0.39
C <sub>10</sub> -DNT-VV	EC, DTS, 500	1.0	0.76
C <sub>10</sub> -DNT-VW	VD, <sup>d</sup> DTS, 500	4.0	3.6
C <sub>10</sub> -DNT-VW	EC, DTS, 500	6.5	4.0
DAT-V	ML, F-DTS, 500	2.0	n.a. <sup>e</sup>
C <sub>10</sub> -TBBT-V	VD, <sup>d</sup> DTS, 200	1.1	1.0
C <sub>10</sub> -TBBT-V	DC, $\beta$ -PTS, 200	4.0	2.0
C <sub>10</sub> -TBBT-V	EC, $\beta$ -PTS, 200	6.2	4.6
$\alpha$ -C <sub>10</sub> -Th-TBBT-V	EC, $\beta$ -PTS, 200	0.55	0.53
$\beta$ -C <sub>10</sub> -Th-TBBT-V	EC, $\beta$ -PTS, 200	2.3	1.6
DNBDT-N	ML, F-DTS, 500	0.06	n.a. <sup>c</sup>
C <sub>10</sub> -DNBDT-NW	EC, $\beta$ -PTS, 100	16	12.1
DNT-W	ML, F-DTS, 500	1.6	n.a. <sup>e</sup>
ChDT	ML, F-DTS, 500	3.1	n.a. <sup>e</sup>
C <sub>10</sub> -ChDT	EC, $\beta$ -PTS, 500	2.6	n.a. <sup>e</sup>
C <sub>10</sub> -Th-ChDT	EC, $\beta$ -PTS, 500	10	n.a. <sup>e</sup>
C <sub>8</sub> -BTBT	EC, DTS, 500	5.0	n.a. <sup>e</sup>
C <sub>10</sub> -DNTT	GC, DTS, 500	11	7.0

<sup>a</sup>ML, manual lamination process; VD, vacuum deposition process; EC, edge-casting process; DC, drop-casting process; GC, gap-casting process. <sup>b</sup> $\mu_{\text{avg}}$  is the average of mobilities for more than 10 devices. <sup>c</sup>Data at substrate temperature ( $T_{\text{sub}}$ ) of room temperature. <sup>d</sup>Data at  $T_{\text{sub}}$  of 100 °C. <sup>e</sup> $\mu_{\text{avg}}$  was not available because a sufficient number of devices was not evaluated.

demonstrated by single-crystalline C<sub>6</sub>-DNT-VW grown using the EC technique. This result was expected based on our transfer integral calculations, because this derivative possessed the largest absolute *t* values in all directions. The other C<sub>10</sub>-DNT-VW derivative exhibited a comparable maximum  $\mu_h$  of 6.5 cm<sup>2</sup> V<sup>-1</sup> s<sup>-1</sup>, whereas C<sub>10</sub>-DNT-VV showed a  $\mu_h$  of 1.0 cm<sup>2</sup> V<sup>-1</sup> s<sup>-1</sup>. Transmission XRD analyses confirmed that thin-film diffractions of the DNT-V series match with their single-crystal packing structures and that their crystal growth direction was along the *b*-axis (column) direction (Figure 7). Polycrystalline thin-film OFETs incorporating C<sub>6</sub>-DNT-VW and C<sub>10</sub>-DNT-VW fabricated by vacuum deposition also demonstrated decent  $\mu_h$  values of 4.0 and 3.7 cm<sup>2</sup> V<sup>-1</sup> s<sup>-1</sup>, respectively. The trend of  $\mu_h$  observed for the DNT-V derivatives was in perfect agreement with their *t* values. Moreover, C<sub>6</sub>-DNT-VW-based transistors demonstrated thermal resistance up to 150 °C.<sup>68</sup>

PVT-grown single crystals of DAT-V were manually laminated on the OFET substrates. In view of the packing motif and charge transport direction of DAT-V, the OFET channel was constructed along the *b*-axis to maximize  $\mu_h$ , with the assistance of in-plane XRD analysis. The highest  $\mu_h$  of 2.0

$\text{cm}^2 \text{V}^{-1} \text{s}^{-1}$  was obtained with DAT-V. When OFET channels were constructed along the *a* axis, a lower  $\mu_{\text{h}}$  of  $1.1 \text{ cm}^2 \text{V}^{-1} \text{s}^{-1}$  was obtained.<sup>71</sup>

The highest  $\mu_{\text{h}}$  of  $6.2 \text{ cm}^2 \text{V}^{-1} \text{s}^{-1}$  was exhibited by the  $\text{C}_{10}$ -TBBT-V single-crystalline OFET, while  $\alpha$ - $\text{C}_{10}$ -Th-TBBT-V and  $\beta$ - $\text{C}_{10}$ -Th-TBBT-V produced mediocre  $\mu_{\text{h}}$  values of 0.55 and  $2.3 \text{ cm}^2 \text{V}^{-1} \text{s}^{-1}$ , respectively. Although the  $\text{C}_{10}$ -TBBT-V device demonstrated a slightly lower  $\mu_{\text{h}}$  than  $\text{C}_{10}$ -DNT-VW ( $6.5 \text{ cm}^2 \text{V}^{-1} \text{s}^{-1}$ ), it showed a lower threshold voltage of  $-20$  to  $-15 \text{ V}$  compared to  $\text{C}_{10}$ -DNT-VW ( $-30$  to  $-25 \text{ V}$ ). In addition,  $\text{C}_{10}$ -TBBT-V demonstrated excellent solution-processability, and the resulting drop-cast thin-film transistor achieved a  $\mu_{\text{h}}$  of  $4.0 \text{ cm}^2 \text{V}^{-1} \text{s}^{-1}$ . Owing to the extended  $\pi$ -conjugation of  $\alpha$ - $\text{C}_{10}$ -Th-TBBT-V and  $\beta$ - $\text{C}_{10}$ -Th-TBBT-V, their transistor devices showed significantly lower threshold voltages of 0 to  $-10 \text{ V}$ , albeit with relatively low  $\mu_{\text{h}}$ . From the transmission XRD data, we confirmed that the solution-processed single-crystalline  $\text{C}_{10}$ -TBBT-V thin film regained its single-crystal packing structure, and that the crystal growth direction was along the *b*-axis, as was also the case for the DNT-V series (column direction, Figure 7).

$\text{C}_{10}$ -DNBDT-NW formed excellent single-crystalline thin films using either the EC technique or the continuous EC technique over large areas.<sup>48–51</sup> Optical microscopic and atomic force microscopy images indicated a smooth crystal surface with steps having a height of one  $\text{C}_{10}$ -DNBDT-NW molecule, indicating well-oriented crystalline films. (Figure 13a,b). Air-stable *p*-channel OFET performance was obtained

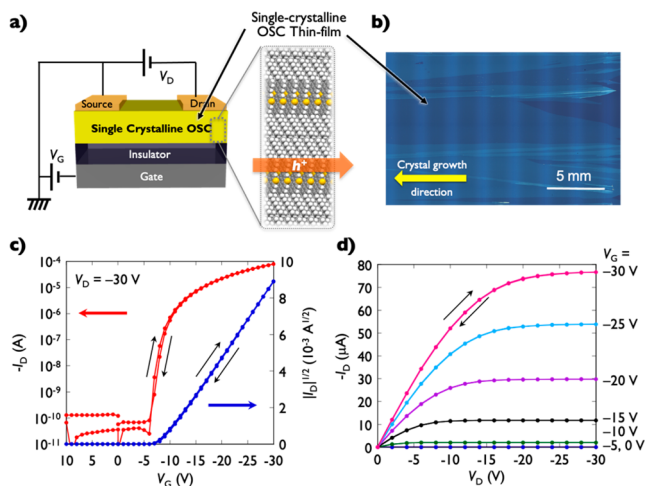


**Figure 13.** (a) Bottom-gate–top-contact device structure and packing structure of  $\text{C}_{10}$ -DNBDT-NW on the substrate and (b) optical microscopy image. (c) Transfer and (d) output characteristics of the OFET based on a  $\text{C}_{10}$ -DNBDT-NW single-crystalline film.

using  $\text{C}_{10}$ -DNBDT-NW with a maximum  $\mu_{\text{h}}$  of  $16 \text{ cm}^2 \text{V}^{-1} \text{s}^{-1}$  (Figure 13c,d). A large on/off ratio of  $10^6$  to  $10^7$  and a small threshold voltage of  $-10$  to  $0 \text{ V}$  were also determined for the  $\text{C}_{10}$ -DNBDT-NW device. The small threshold voltage for this material can be attributed to its low IP value (5.24 eV) resulting from the extended  $\pi$ -conjugated core. Moreover,  $\text{C}_{10}$ -DNBDT-NW-based transistors demonstrated higher thermal resistance up to  $200 \text{ }^\circ\text{C}$ . In addition, Hall effect measurements suggested significant hole diffusion. Thus, the  $\text{C}_{10}$ -DNBDT-NW-based OSC exhibited a band transport mechanism with delocalized charge-carriers over the OSC layer.<sup>94,95</sup> Furthermore, we have recently reported that bending a flexible device

incorporating a  $\text{C}_{10}$ -DNBDT-NW single-crystalline film caused uniaxial lattice compression and led to a mobility increase of 70% under 3% strain. An in-depth analysis showed that this compression suppresses molecular motion.<sup>96</sup>

DNT-W afforded flat platelet crystals when employing PVT, which could be simply laminated on substrates for OFET evaluation. The resulting DNT-W-based OFETs exhibited typical *p*-channel transfer and output characteristics with negligible hysteresis and an air-stable  $\mu_{\text{h}}$  of  $1.6 \text{ cm}^2 \text{V}^{-1} \text{s}^{-1}$ . Despite the encouraging results obtained from our first second-generation zigzag-shaped DNT-W, the associated OFET suffered from a substantial threshold voltage ( $-50 \text{ V}$ ), a high injection barrier between the gold electrode and the semiconductor layer (due to the large IP value of 5.87 eV), and a  $\mu_{\text{h}}$  insufficient for high-performance electronics. Recently, Yasuda and co-workers developed an original synthetic route for  $\text{C}_8$ -substituted dinaphtho[1,2-*b*:2',1-*d'*]chalcogenophenes (DNE), including dinaphtho[1,2-*b*:2',1-*d'*]thiophene (DNT), dinaphtho[1,2-*b*:2',1-*d'*]selenophene (DNS), and dinaphtho[1,2-*b*:2',1-*d'*]tellurophene (DNTe).<sup>97</sup> Incorporation of the alkyl chain increased the solubility of these DNE derivatives such that solution-processing for device fabrication was viable. The introduction of tellurium in DNTe also effectively lowered its IP value to 5.24 eV. However, the threshold voltages of the  $\text{C}_8$ -DNE series remained high.

In the case of the extended zigzag-shaped ChDT  $\pi$ -core, a decent  $\mu_{\text{h}}$  of  $3.1 \text{ cm}^2 \text{V}^{-1} \text{s}^{-1}$  was obtained from a single-crystalline thin film by the ML technique. It is worth noting that the threshold voltage for ChDT ( $-25 \text{ V}$ ) was found to be significantly improved compared to that for DNT-W due to its extended  $\pi$ -conjugation.  $\text{C}_{10}$ -ChDT and  $\text{C}_{10}$ -Th-ChDT both formed well-oriented single-crystalline thin films with smooth surfaces when applying the EC technique and showed maximum  $\mu_{\text{h}}$  values of 2.6 and  $10 \text{ cm}^2 \text{V}^{-1} \text{s}^{-1}$ , respectively. The high  $\mu_{\text{h}}$  exhibited by these ChDT derivatives may be correlated with their low  $\Delta t$  values, that the  $\pi$ -core is insensitive to detrimental molecular motions and shows consistent intermolecular orbital overlaps.

Thermal stress test of high-mobility  $\text{C}_{10}$ -DNBDT-NW OSCs using solution-processed single-crystalline films on silicon substrates at  $200 \text{ }^\circ\text{C}$ , were performed in transistors. To evaluate the thermal durability of  $\text{C}_{10}$ -DNBDT-NW accurately, the transistors were prepared as follows: (1) The solution-processed single-crystalline films prepared by the edge-casting method were annealed at  $200 \text{ }^\circ\text{C}$  for 10 min under nitrogen conditions. (2) After the film cooled to room temperature, the  $\text{F}_4$ -TCNQ and gold electrodes were deposited. Notably, it was found that the mobility was unchanged, while the threshold voltage showed a slight positive shift. This might be due to the decrement of channel traps such as water and oxygen by annealing at high temperature. As a comparison, the other transistor was annealed at the same temperature after the  $\text{F}_4$ -TCNQ and gold electrodes were deposited. In this case, the mobility was slightly decreased. This result might be attributed to the morphology change at the interface between OSC and  $\text{F}_4$ -TCNQ. Therefore, the solution-processed single-crystalline film of  $\text{C}_{10}$ -DNBDT-NW possesses thermal durability over  $200 \text{ }^\circ\text{C}$ .

## CONCLUSIONS AND FUTURE PERSPECTIVES

In this Perspective, we have summarized recent advances in the development of bent-shaped OSCs for OFET applications.

The bent-shaped molecules presented herein all demonstrated an excellent distribution of HOMO coefficients, leading to effective intermolecular orbital overlaps as well as electronic structures suitable for air-stable *p*-type OFET operation and charge injection. The incorporation of sulfur leads to a large HOMO coefficient for the sulfur atom that induces various heteroatom interactions and contributes to the reinforcement of the favorable HB packing structure in the solid state. It is apparent that the bent-shaped geometry contributes to the stabilization of the crystal phases of the OSCs, resulting in high thermal durability. Our work with V-shaped OSCs having bent-shaped geometries has mitigated various challenges associated with these compounds, such as low IP values, high OFET threshold voltages, poor thermal durability, and moderate charge mobilities. This was accomplished by extending the length of  $\pi$ -conjugation and alternating the type of bent shape. These endeavors provided a *p*-channel OFET mobility of  $16 \text{ cm}^2 \text{ V}^{-1} \text{ s}^{-1}$  in conjunction with N-shaped OSCs, which is adequate for the development of applications such as radio frequency identifier tags. However, the performance of OSCs in transistors is still far inferior to that of inorganic semiconductors, such that OSCs remain best suited to applications in relatively low-end electronics. In addition, the range of high-performance electron-transporting *n*-type OSCs is still limited, and so there is an urgent need for the development of all-organic complementary logic circuits. To improve the carrier mobility for both *p*- and *n*-type OSCs, it is necessary to form a clearer understanding of molecular motion by studying OSCs that exhibit band-transport characteristics using techniques such as Raman spectroscopy, infrared spectroscopy, and neutron scattering. It is our hope that the bent-shaped OSCs described herein will provide insights into the design of molecular geometries and orbital configurations that are suitable for the advancement of the air-stable, thermally durable, high-performance *n*-type OSCs required for next-generation electronic materials.

## ■ ASSOCIATED CONTENT

### SI Supporting Information

The Supporting Information is available free of charge at <https://pubs.acs.org/doi/10.1021/jacs.9b10450>.

Video demonstrating the edge-casting technique (AVI)

## ■ AUTHOR INFORMATION

### Corresponding Author

**Toshihiro Okamoto** – Material Innovation Research Center (MIRC) and Department of Advanced Materials Science, Graduate School of Frontier Sciences, The University of Tokyo, Kashiwa, Chiba 277-8561, Japan; University of Tokyo Advanced Operando-Measurement Technology Open Innovation Laboratory (OPERANDO-OIL), National Institute of Advanced Industrial Science and Technology (AIST), Kashiwa, Chiba 277-8561, Japan; PRESTO, JST, Kawaguchi, Saitama 332-0012, Japan; [orcid.org/0000-0002-4783-0621](https://orcid.org/0000-0002-4783-0621); Email: [tokamoto@edu.k.u-tokyo.ac.jp](mailto:tokamoto@edu.k.u-tokyo.ac.jp)

### Authors

**Craig P. Yu** – Material Innovation Research Center (MIRC) and Department of Advanced Materials Science, Graduate School of Frontier Sciences, The University of Tokyo, Kashiwa, Chiba 277-8561, Japan; [orcid.org/0000-0002-1423-5244](https://orcid.org/0000-0002-1423-5244)

**Chikahiko Mitsui** – Material Innovation Research Center (MIRC) and Department of Advanced Materials Science, Graduate School of Frontier Sciences, The University of Tokyo, Kashiwa, Chiba 277-8561, Japan

**Masakazu Yamagishi** – Department of Applied Chemistry and Chemical Engineering, National Institute of Technology, Toyama College, Toyama City, Toyama 939-8630, Japan

**Hiroyuki Ishii** – Department of Applied Physics, Faculty of Pure and Applied Sciences, University of Tsukuba, Tsukuba, Ibaraki 305-8573, Japan; [orcid.org/0000-0003-0644-1424](https://orcid.org/0000-0003-0644-1424)

**Jun Takeya** – Material Innovation Research Center (MIRC) and Department of Advanced Materials Science, Graduate School of Frontier Sciences, The University of Tokyo, Kashiwa, Chiba 277-8561, Japan; University of Tokyo Advanced Operando-Measurement Technology Open Innovation Laboratory (OPERANDO-OIL), National Institute of Advanced Industrial Science and Technology (AIST), Kashiwa, Chiba 277-8561, Japan; MANA, National Institute for Materials Science (NIMS), Tsukuba 205-0044, Japan

Complete contact information is available at: <https://pubs.acs.org/10.1021/jacs.9b10450>

### Notes

The authors declare no competing financial interest.

## ■ ACKNOWLEDGMENTS

This work was supported by the Japan Science and Technology Agency (JST) PRESTO programs “Molecular Technology and Creation of New Functions” (grant JPMJPR13K5 and JPMJPR12K2) and “Scientific Innovation for Energy Harvesting Technology” (grant JPMJPR17R2) as well as a Japan Society for the Promotion of Science (JSPS) KAKENHI grant-in-aid for Scientific Research B (no. 17H03104). C.P.Y. would also like to acknowledge support for his graduate work through a Todai Fellowship at the University of Tokyo. Finally, the authors thank R. Wang for performing additional DFT calculations.

## ■ REFERENCES

- (1) Bao, Z.; Locklin, J. *Organic Field-Effect Transistors*, 1st ed.; CRC Press: Boca Raton, FL, 2007.
- (2) Wang, C.; Dong, H.; Hu, W.; Liu, Y.; Zhu, D. Semiconducting  $\pi$ -Conjugated Systems in Field-Effect Transistors: A Material Odyssey of Organic Electronics. *Chem. Rev.* **2012**, *112*, 2208–2267.
- (3) Root, S. E.; Savagatrup, S.; Printz, A. D.; Rodriguez, D.; Lipomi, D. J. Mechanical Properties of Organic Semiconductors for Stretchable, Highly Flexible, and Mechanically Robust Electronics. *Chem. Rev.* **2017**, *117*, 6467–6499.
- (4) Mei, J.; Diao, Y.; Appleton, A. L.; Fang, L.; Bao, Z. Integrated Materials Design of Organic Semiconductors for Field-Effect Transistors. *J. Am. Chem. Soc.* **2013**, *135*, 6724–6746.
- (5) Müllen, K.; Scherf, U. *Organic Light-Emitting Devices: Synthesis, Properties and Applications*; Wiley-VCH, 2006.
- (6) Burn, P. L.; Lo, S.-C.; Samuel, I. D. W. The Development of Light-Emitting Dendrimers for Displays. *Adv. Mater.* **2007**, *19*, 1675–1688.
- (7) Ostroverkhova, O. Organic Optoelectronic Materials: Mechanisms and Applications. *Chem. Rev.* **2016**, *116*, 13279–13412.
- (8) Thompson, B. C.; Fréchet, J. M. J. Polymer-Fullerene Composite Solar Cells. *Angew. Chem., Int. Ed.* **2008**, *47*, 58–77.
- (9) Günes, S.; Neugebauer, H.; Sariciftci, N. S. Conjugated Polymer-Based Organic Solar Cells. *Chem. Rev.* **2007**, *107*, 1324–1338.
- (10) Son, H. J.; He, F.; Carsten, B.; Yu, L. Are we there yet? Design of better conjugated polymers for polymer solar cells. *J. Mater. Chem.* **2011**, *21*, 18934–18945.

- (11) Cheng, Y.-J.; Yang, S.-H.; Hsu, C.-S. Synthesis of Conjugated Polymers for Organic Solar Cell Applications. *Chem. Rev.* **2009**, *109*, 5868–5923.
- (12) Chen, Y.; Zhao, Y.; Liang, Z. Solution processed organic thermoelectrics: towards flexible thermoelectric modules. *Energy Environ. Sci.* **2015**, *8*, 401–422.
- (13) Park, T.; Park, C.; Kim, B.; Shin, H.; Kim, E. Flexible PEDOT electrodes with large thermoelectric power factors to generate electricity by the touch of fingertips. *Energy Environ. Sci.* **2013**, *6*, 788–792.
- (14) Shi, K.; Zhang, F.; Di, C.-A.; Yan, T.-W.; Zou, Y.; Zhou, X.; Zhu, D.; Wang, J.-Y.; Pei, J. Toward High Performance n-Type Thermoelectric Materials by Rational Modification of BDPPV Backbones. *J. Am. Chem. Soc.* **2015**, *137*, 6979–6982.
- (15) Schlitz, R. A.; Brunetti, F. G.; Glauddell, A. M.; Miller, P. L.; Brady, M. A.; Takacs, C. J.; Hawker, C. J.; Chabynyc, M. L. Solubility-Limited Extrinsic n-Type Doping of a High Electron Mobility Polymer for Thermoelectric Applications. *Adv. Mater.* **2014**, *26*, 2825–2830.
- (16) Lavieville, R.; Zhang, Y.; Casu, A.; Genovese, A.; Manna, L.; Di Fabrizio, E.; Krahn, R. Charge Transport in Nanoscale “All-Inorganic” Networks of Semiconductor Nanorods Linked by Metal Domains. *ACS Nano* **2012**, *6*, 2940–2947.
- (17) Anthony, J. E. Functionalized Acenes and Heteroacenes for Organic Electronics. *Chem. Rev.* **2006**, *106*, 5028–5048.
- (18) Coropceanu, V.; Cornil, J.; da Silva Filho, D. A.; Olivier, Y.; Silbey, R.; Brédas, J.-L. Charge Transport in Organic Semiconductors. *Chem. Rev.* **2007**, *107*, 926–952.
- (19) Takimiya, K.; Shinamura, S.; Osaka, I.; Miyazaki, E. Thienoacene-Based Organic Semiconductors. *Adv. Mater.* **2011**, *23*, 4347–4370.
- (20) Liu, C.; Huang, K.; Park, W.-T.; Li, M.; Yang, T.; Liu, X.; Liang, L.; Minari, T.; Noh, Y.-Y. A unified understanding of charge transport in organic semiconductors: the importance of attenuated delocalization for the carriers. *Mater. Horiz.* **2017**, *4*, 608–618.
- (21) Ji, L.-F.; Fan, J.-X.; Qin, G.-Y.; Zhang, N.-X.; Lin, P.-P.; Ren, A.-M. Theoretical Study on the Electronic Structures and Charge Transport Properties of a Series of Rubrene Derivatives. *J. Phys. Chem. C* **2018**, *122*, 21226–21238.
- (22) Wang, Y.; Sun, L.; Wang, C.; Yang, F.; Ren, X.; Zhang, X.; Dong, H.; Hu, W. Organic crystalline materials in flexible electronics. *Chem. Soc. Rev.* **2019**, *48*, 1492–1530.
- (23) Gryn'ova, G.; Lin, K.-H.; Corminboeuf, C. Read between the Molecules: Computational Insights into Organic Semiconductors. *J. Am. Chem. Soc.* **2018**, *140*, 16370–16386.
- (24) McGarry, K. A.; Xie, W.; Sutton, C.; Risko, C.; Wu, Y.; Young, V. G.; Brédas, J.-L.; Frisbie, C. D.; Douglas, C. J. Rubrene-Based Single-Crystal Organic Semiconductors: Synthesis, Electronic Structure, and Charge-Transport Properties. *Chem. Mater.* **2013**, *25*, 2254–2263.
- (25) Giri, G.; Verploegen, E.; Mannsfeld, S. C. B.; Atahan-Evrenk, S.; Kim, D. H.; Lee, S. Y.; Becerril, H. A.; Aspuru-Guzik, A.; Toney, M. F.; Bao, Z. Tuning charge transport in solution-sheared organic semiconductors using lattice strain. *Nature* **2011**, *480*, 504.
- (26) Rühle, V.; Lukyanov, A.; May, F.; Schrader, M.; Vehoff, T.; Kirkpatrick, J.; Baumeier, B.; Andrienko, D. Microscopic Simulations of Charge Transport in Disordered Organic Semiconductors. *J. Chem. Theory Comput.* **2011**, *7*, 3335–3345.
- (27) Nomura, K.; Ohta, H.; Takagi, A.; Kamiya, T.; Hirano, M.; Hosono, H. Room-temperature fabrication of transparent flexible thin-film transistors using amorphous oxide semiconductors. *Nature* **2004**, *432*, 488–492.
- (28) Kuribara, K.; Wang, H.; Uchiyama, N.; Fukuda, K.; Yokota, T.; Zschieschang, U.; Jaye, C.; Fischer, D.; Klauk, H.; Yamamoto, T.; Takimiya, K.; Ikeda, M.; Kuwabara, H.; Sekitani, T.; Loo, Y.-L.; Someya, T. Organic transistors with high thermal stability for medical applications. *Nat. Commun.* **2012**, *3*, 723.
- (29) Payne, M. M.; Parkin, S. R.; Anthony, J. E. Functionalized Higher Acenes: Hexacene and Heptacene. *J. Am. Chem. Soc.* **2005**, *127*, 8028–8029.
- (30) Tang, M. L.; Okamoto, T.; Bao, Z. High-Performance Organic Semiconductors: Asymmetric Linear Acenes Containing Sulphur. *J. Am. Chem. Soc.* **2006**, *128*, 16002–16003.
- (31) Wong, M. Y.; Hedley, G. J.; Xie, G.; Kölln, L. S.; Samuel, I. D. W.; Pertegás, A.; Bolink, H. J.; Zysman-Colman, E. Light-Emitting Electrochemical Cells and Solution-Processed Organic Light-Emitting Diodes Using Small Molecule Organic Thermally Activated Delayed Fluorescence Emitters. *Chem. Mater.* **2015**, *27*, 6535–6542.
- (32) Bin, H.; Yang, Y.; Zhang, Z.-G.; Ye, L.; Ghasemi, M.; Chen, S.; Zhang, Y.; Zhang, C.; Sun, C.; Xue, L.; Yang, C.; Ade, H.; Li, Y. 9.73% Efficiency Nonfullerene All Organic Small Molecule Solar Cells with Absorption-Complementary Donor and Acceptor. *J. Am. Chem. Soc.* **2017**, *139*, 5085–5094.
- (33) Lin, L.-Y.; Chen, Y.-H.; Huang, Z.-Y.; Lin, H.-W.; Chou, S.-H.; Lin, F.; Chen, C.-W.; Liu, Y.-H.; Wong, K.-T. A Low-Energy-Gap Organic Dye for High-Performance Small-Molecule Organic Solar Cells. *J. Am. Chem. Soc.* **2011**, *133*, 15822–15825.
- (34) Sun, Y.; Welch, G. C.; Leong, W. L.; Takacs, C. J.; Bazan, G. C.; Heeger, A. J. Solution-processed small-molecule solar cells with 6.7% efficiency. *Nat. Mater.* **2012**, *11*, 44.
- (35) Maliakal, A.; Raghavachari, K.; Katz, H.; Chandross, E.; Siegrist, T. Photochemical Stability of Pentacene and a Substituted Pentacene in Solution and in Thin Films. *Chem. Mater.* **2004**, *16*, 4980–4986.
- (36) Laquindanum, J. G.; Katz, H. E.; Lovinger, A. J. Synthesis, Morphology, and Field-Effect Mobility of Anthradithiophenes. *J. Am. Chem. Soc.* **1998**, *120*, 664–672.
- (37) Mishra, A.; Bäuerle, P. Small Molecule Organic Semiconductors on the Move: Promises for Future Solar Energy Technology. *Angew. Chem., Int. Ed.* **2012**, *51*, 2020–2067.
- (38) Leung, L. M.; Lo, W. Y.; So, S. K.; Lee, K. M.; Choi, W. K. A High-Efficiency Blue Emitter for Small Molecule-Based Organic Light-Emitting Diode. *J. Am. Chem. Soc.* **2000**, *122*, 5640–5641.
- (39) Kulkarni, A. P.; Tonzola, C. J.; Babel, A.; Jenekhe, S. A. Electron Transport Materials for Organic Light-Emitting Diodes. *Chem. Mater.* **2004**, *16*, 4556–4573.
- (40) Liu, Y.; Li, C.; Ren, Z.; Yan, S.; Bryce, M. R. All-organic thermally activated delayed fluorescence materials for organic light-emitting diodes. *Nat. Rev. Mater.* **2018**, *3*, 18020.
- (41) Klauk, H.; Halik, M.; Zschieschang, U.; Schmid, G.; Radlik, W.; Weber, W. High-mobility polymer gate dielectric pentacene thin film transistors. *J. Appl. Phys.* **2002**, *92*, 5259–5263.
- (42) Ebata, H.; Izawa, T.; Miyazaki, E.; Takimiya, K.; Ikeda, M.; Kuwabara, H.; Yui, T. Highly Soluble [1]Benzothieno[3,2-b]benzothiophene (BTBT) Derivatives for High-Performance, Solution-Processed Organic Field-Effect Transistors. *J. Am. Chem. Soc.* **2007**, *129*, 15732–15733.
- (43) Yamamoto, T.; Takimiya, K. Facile Synthesis of Highly  $\pi$ -Extended Heteroarenes, Dinaphtho[2,3-b:2',3'-f]chalcogenopheno[3,2-b]chalcogenophenes, and Their Application to Field-Effect Transistors. *J. Am. Chem. Soc.* **2007**, *129*, 2224–2225.
- (44) Wang, C.; Dong, H.; Hu, W.; Liu, Y.; Zhu, D. Semiconducting  $\pi$ -Conjugated Systems in Field-Effect Transistors: A Material Odyssey of Organic Electronics. *Chem. Rev.* **2012**, *112*, 2208–2267.
- (45) Curtis, M. D.; Cao, J.; Kampf, J. W. Solid-State Packing of Conjugated Oligomers: From  $\pi$ -Stacks to the Herringbone Structure. *J. Am. Chem. Soc.* **2004**, *126*, 4318–4328.
- (46) Purushothaman, B.; Bruzek, M.; Parkin, S. R.; Miller, A.-F.; Anthony, J. E. Synthesis and Structural Characterization of Crystalline Nonacenes. *Angew. Chem., Int. Ed.* **2011**, *50*, 7013–7017.
- (47) Anthony, J. E. The Larger Acenes: Versatile Organic Semiconductors. *Angew. Chem., Int. Ed.* **2008**, *47*, 452–483.
- (48) Uemura, T.; Hirose, Y.; Uno, M.; Takimiya, K.; Takeya, J. Very High Mobility in Solution-Processed Organic Thin-Film Transistors of Highly Ordered [1]Benzothieno[3,2-b]benzothiophene Derivatives. *Appl. Phys. Express* **2009**, *2*, 111501.

- (49) Soeda, J.; Uemura, T.; Okamoto, T.; Mitsui, C.; Yamagishi, M.; Takeya, J. Inch-Size Solution-Processed Single-Crystalline Films of High-Mobility Organic Semiconductors. *Appl. Phys. Express* **2013**, *6*, 076503.
- (50) Yamamura, A.; Watanabe, S.; Uno, M.; Mitani, M.; Mitsui, C.; Tsurumi, J.; Isahaya, N.; Kanaoka, Y.; Okamoto, T.; Takeya, J. Wafer-scale, layer-controlled organic single crystals for high-speed circuit operation. *Sci. Adv.* **2018**, *4*, No. eao5758.
- (51) Yamamura, A.; Matsui, H.; Uno, M.; Isahaya, N.; Tanaka, Y.; Kudo, M.; Ito, M.; Mitsui, C.; Okamoto, T.; Takeya, J. Painting Integrated Complementary Logic Circuits for Single-Crystal Organic Transistors: A Demonstration of a Digital Wireless Communication Sensing Tag. *Adv. Electron. Mater.* **2017**, *3*, 1600456.
- (52) Kang, M. J.; Doi, I.; Mori, H.; Miyazaki, E.; Takimiya, K.; Ikeda, M.; Kuwabara, H. Alkylated Dinaphtho[2,3-b:2',3'-f]Thieno[3,2-b]Thiophenes (Cn-DNTTs): Organic Semiconductors for High-Performance Thin-Film Transistors. *Adv. Mater.* **2011**, *23*, 1222–1225.
- (53) Iino, H.; Usui, T.; Hanna, J.-i. Liquid crystals for organic thin-film transistors. *Nat. Commun.* **2015**, *6*, 6828.
- (54) Inoue, S.; Minemawari, H.; Tsutsumi, J. y.; Chikamatsu, M.; Yamada, T.; Horiuchi, S.; Tanaka, M.; Kumai, R.; Yoneya, M.; Hasegawa, T. Effects of Substituted Alkyl Chain Length on Solution-Processable Layered Organic Semiconductor Crystals. *Chem. Mater.* **2015**, *27*, 3809–3812.
- (55) He, K.; Li, W.; Tian, H.; Zhang, J.; Yan, D.; Geng, Y.; Wang, F. Asymmetric Conjugated Molecules Based on [1]Benzo[thieno][3,2-b][1]benzothiophene for High-Mobility Organic Thin-Film Transistors: Influence of Alkyl Chain Length. *ACS Appl. Mater. Interfaces* **2017**, *9*, 35427–35436.
- (56) Grigoriadis, C.; Niebel, C.; Ruzié, C.; Geerts, Y. H.; Floudas, G. Order, Viscoelastic, and Dielectric Properties of Symmetric and Asymmetric Alkyl[1]benzo[thieno][3,2-b][1]benzothiophenes. *J. Phys. Chem. B* **2014**, *118*, 1443–1451.
- (57) Inoue, S.; Shinamura, S.; Sadamitsu, Y.; Arai, S.; Horiuchi, S.; Yoneya, M.; Takimiya, K.; Hasegawa, T. Extended and Modulated Thienothiophenes for Thermally Durable and Solution-Processable Organic Semiconductors. *Chem. Mater.* **2018**, *30*, 5050–5060.
- (58) Diaó, Y.; Tee, B. C. K.; Giri, G.; Xu, J.; Kim, D. H.; Becerril, H. A.; Stoltenberg, R. M.; Lee, T. H.; Xue, G.; Mannsfeld, S. C. B.; Bao, Z. Solution coating of large-area organic semiconductor thin films with aligned single-crystalline domains. *Nat. Mater.* **2013**, *12*, 665.
- (59) Nakayama, K.; Hirose, Y.; Soeda, J.; Yoshizumi, M.; Uemura, T.; Uno, M.; Li, W.; Kang, M. J.; Yamagishi, M.; Okada, Y.; Miyazaki, E.; Nakazawa, Y.; Nakao, A.; Takimiya, K.; Takeya, J. Patternable Solution-Crystallized Organic Transistors with High Charge Carrier Mobility. *Adv. Mater.* **2011**, *23*, 1626–1629.
- (60) Yuan, Y.; Giri, G.; Ayzner, A. L.; Zoombelt, A. P.; Mannsfeld, S. C. B.; Chen, J.; Nordlund, D.; Toney, M. F.; Huang, J.; Bao, Z. Ultra-high mobility transparent organic thin film transistors grown by an off-centre spin-coating method. *Nat. Commun.* **2014**, *5*, 3005.
- (61) Iino, H.; Kobori, T.; Hanna, J.-i. Improved thermal stability in organic FET fabricated with a soluble BTBT derivative. *J. Non-Cryst. Solids* **2012**, *358*, 2516–2519.
- (62) Okamoto, K.; Kawamura, T.; Sone, M.; Ogino, K. Study on liquid crystallinity in 2,9-dialkylpentacenes. *Liq. Cryst.* **2007**, *34*, 1001–1007.
- (63) Kuwabara, H.; Ikeda, M.; Takimiya, K. U.S. Patent 2011/0303910 A1, 2010.
- (64) Fratini, S.; Ciuchi, S.; Mayou, D.; de Laissardière, G. T.; Troisi, A. A map of high-mobility molecular semiconductors. *Nat. Mater.* **2017**, *16*, 998.
- (65) Troisi, A.; Orlandi, G.; Anthony, J. E. Electronic Interactions and Thermal Disorder in Molecular Crystals Containing Cofacial Pentacene Units. *Chem. Mater.* **2005**, *17*, 5024–5031.
- (66) Ciuchi, S.; Fratini, S. Electronic transport and quantum localization effects in organic semiconductors. *Phys. Rev. B: Condens. Matter Mater. Phys.* **2012**, *86*, 245201.
- (67) Illig, S.; Eggeman, A. S.; Troisi, A.; Jiang, L.; Warwick, C.; Nikolka, M.; Schweicher, G.; Yeates, S. G.; Henri Geerts, Y.; Anthony, J. E.; Sirringhaus, H. Reducing dynamic disorder in small-molecule organic semiconductors by suppressing large-amplitude thermal motions. *Nat. Commun.* **2016**, *7*, 10736.
- (68) Okamoto, T.; Mitsui, C.; Yamagishi, M.; Nakahara, K.; Soeda, J.; Hirose, Y.; Miwa, K.; Sato, H.; Yamano, A.; Matsushita, T.; Uemura, T.; Takeya, J. V-shaped organic semiconductors with solution processability, high mobility, and high thermal durability. *Adv. Mater.* **2013**, *25*, 6392–6397.
- (69) Mitsui, C.; Okamoto, T.; Matsui, H.; Yamagishi, M.; Matsushita, T.; Soeda, J.; Miwa, K.; Sato, H.; Yamano, A.; Uemura, T.; Takeya, J. Dinaphtho[1,2b:2',1'd]chalcogenophenes: Comprehensive Investigation of the Effect of the Chalcogen Atoms in the Phenacene-Type  $\pi$  Electronic Cores. *Chem. Mater.* **2013**, *25*, 3952–3956.
- (70) Mitsui, C.; Okamoto, T.; Yamagishi, M.; Tsurumi, J.; Yoshimoto, K.; Nakahara, K.; Soeda, J.; Hirose, Y.; Sato, H.; Yamano, A.; Uemura, T.; Takeya, J. High-performance solution-processable N-shaped organic semiconducting materials with stabilized crystal phase. *Adv. Mater.* **2014**, *26*, 4546–4551.
- (71) Mitsui, C.; Yamagishi, M.; Shikata, R.; Ishii, H.; Matsushita, T.; Nakahara, K.; Yano, M.; Sato, H.; Yamano, A.; Takeya, J.; Okamoto, T. Oxygen- and sulfur-bridged bianthracene V-shaped organic semiconductors. *Bull. Chem. Soc. Jpn.* **2017**, *90*, 931–938.
- (72) Mitsui, C.; Tsuyama, H.; Shikata, R.; Murata, Y.; Kuniyasu, H.; Yamagishi, M.; Ishii, H.; Yamamoto, A.; Hirose, Y.; Yano, M.; Takehara, T.; Suzuki, T.; Sato, H.; Yamano, A.; Fukuzaki, E.; Watanabe, T.; Usami, Y.; Takeya, J.; Okamoto, T. High performance solution-crystallized thin-film transistors based on V-shaped thieno[3,2-f:4,5-f']bis[1]benzothiophene semiconductors. *J. Mater. Chem. C* **2017**, *5*, 1903–1909.
- (73) Yamamoto, A.; Murata, Y.; Mitsui, C.; Ishii, H.; Yamagishi, M.; Yano, M.; Sato, H.; Yamano, A.; Takeya, J.; Okamoto, T. Zigzag-Elongated Fused  $\pi$ -Electronic Core: A Molecular Design Strategy to Maximize Charge-Carrier Mobility. *Adv. Sci.* **2018**, *5*, 1700317.
- (74) Tsurumi, J.; Matsui, H.; Kubo, T.; Hausermann, R.; Mitsui, C.; Okamoto, T.; Watanabe, S.; Takeya, J. Coexistence of ultra-long spin relaxation time and coherent charge transport in organic single-crystal semiconductors. *Nat. Phys.* **2017**, *13*, 994–998.
- (75) Solubility Parameter. *Bulletin of the American Group; International Institute for Conservation of Historic and Artistic Works*, 1968; Vol. 8, pp 20–24.
- (76) The reorganization energy was calculated based on the optimized structure by DFT at the B3LYP/6-31G(d) level.
- (77) Schleyer, P. v. R.; Maerker, C.; Dransfeld, A.; Jiao, H.; van Eikema Hommes, N. J. R. Nucleus-Independent Chemical Shifts: A Simple and Efficient Aromaticity Probe. *J. Am. Chem. Soc.* **1996**, *118*, 6317–6318.
- (78) Chen, Z.; Wannere, C. S.; Corminboeuf, C.; Puchta, R.; Schleyer, P. v. R. Nucleus-Independent Chemical Shifts (NICS) as an Aromaticity Criterion. *Chem. Rev.* **2005**, *105*, 3842–3888.
- (79) Münzel, N.; Kesper, K.; Schweig, A.; Specht, H. Detection of 2,5-dimethylene-2,5-dihydrothiophene and thiophenoradialene. *Tetrahedron Lett.* **1988**, *29*, 6239–6242.
- (80) Okamoto, H.; Kawasaki, N.; Kaji, Y.; Kubozono, Y.; Fujiwara, A.; Yamaji, M. Air-assisted High-performance Field-effect Transistor with Thin Films of Picene. *J. Am. Chem. Soc.* **2008**, *130*, 10470–10471.
- (81) Kawai, N.; Eguchi, R.; Goto, H.; Akaike, K.; Kaji, Y.; Kambe, T.; Fujiwara, A.; Kubozono, Y. Characteristics of Single Crystal Field-Effect Transistors with a New Type of Aromatic Hydrocarbon, Picene. *J. Phys. Chem. C* **2012**, *116*, 7983–7988.
- (82) De, A.; Ghosh, R.; Roychowdhury, S.; Roychowdhury, P. Structural analysis of picene, C<sub>22</sub>H<sub>14</sub>. *Acta Crystallogr., Sect. C: Cryst. Struct. Commun.* **1985**, *41*, 907–909.
- (83) Tedjamulia, M. L.; Tominaga, Y.; Castle, R. N.; Lee, M. L. The synthesis of dinaphthothiophenes. *J. Heterocyclic Chem.* **1983**, *20*, 1143–1148.

(84) Lloyd-Jones, G. C.; Moseley, J. D.; Renny, J. S. Mechanism and Application of the Newman-Kwart O→S Rearrangement of O-Aryl Thiocarbamates. *Synthesis* **2008**, *2008*, 661–689.

(85) Matsuoka, M.; Iwamoto, A.; Kitao, T. Reaction of 2, 3-dichloro-1, 4-naphthoquinone with dithiooxamide. Synthesis of dibenzo[b, i]thianthrene-5, 7, 12, 14-tetrone. *J. Heterocycl. Chem.* **1991**, *28*, 1445–1447.

(86) De, P. K.; Neckers, D. C. Sulfur Containing Stable Unsubstituted Heptacene Analogs. *Org. Lett.* **2012**, *14*, 78–81.

(87) Wex, B.; Kaafarani, B. R.; Kirschbaum, K.; Neckers, D. C. Synthesis of the anti and syn Isomers of Thieno[f, f']bis[1]-benzothiophene. Comparison of the Optical and Electrochemical Properties of the anti and syn Isomers. *J. Org. Chem.* **2005**, *70*, 4502–4505.

(88) Armarego, W. L. F. The synthesis of two dinaphthothiophens. *J. Chem. Soc.* **1960**, 433–436.

(89) Shinamura, S.; Osaka, I.; Miyazaki, E.; Nakao, A.; Yamagishi, M.; Takeya, J.; Takimiya, K. Linear- and Angular-Shaped Naphthodithiophenes: Selective Synthesis, Properties, and Application to Organic Field-Effect Transistors. *J. Am. Chem. Soc.* **2011**, *133*, 5024–5035.

(90) Mamane, V.; Hannen, P.; Fürstner, A. Synthesis of Phenanthrenes and Polycyclic Heteroarenes by Transition-Metal Catalyzed Cycloisomerization Reactions. *Chem. - Eur. J.* **2004**, *10*, 4556–4575.

(91) Laudise, R. A.; Kloc, C.; Simpkins, P. G.; Siegrist, T. Physical vapor growth of organic semiconductors. *J. Cryst. Growth* **1998**, *187*, 449–454.

(92) Kloc, C.; Simpkins, P. G.; Siegrist, T.; Laudise, R. A. Physical vapor growth of centimeter-sized crystals of  $\alpha$ -hexathiophene. *J. Cryst. Growth* **1997**, *182*, 416–427.

(93) Izawa, T.; Miyazaki, E.; Takimiya, K. Molecular Ordering of High-Performance Soluble Molecular Semiconductors and Re-evaluation of Their Field-Effect Transistor Characteristics. *Adv. Mater.* **2008**, *20*, 3388–3392.

(94) Takeya, J.; Tsukagoshi, K.; Aoyagi, Y.; Takenobu, T.; Iwasa, Y. Hall Effect of Quasi-Hole Gas in Organic Single-Crystal Transistors. *Jpn. J. Appl. Phys.* **2005**, *44*, L1393–L1396.

(95) Podzorov, V.; Menard, E.; Rogers, J. A.; Gershenson, M. E. Hall Effect in the Accumulation Layers on the Surface of Organic Semiconductors. *Phys. Rev. Lett.* **2005**, *95*, 226601.

(96) Kubo, T.; Haeusermann, R.; Tsurumi, J.; Soeda, J.; Okada, Y.; Yamashita, Y.; Akamatsu, N.; Shishido, A.; Mitsui, C.; Okamoto, T.; Yanagisawa, S.; Matsui, H.; Takeya, J. Suppressing molecular vibrations in organic semiconductors by inducing strain. *Nat. Commun.* **2016**, *7*, 11156.

(97) Oyama, T.; Yang, Y. S.; Matsuo, K.; Yasuda, T. Effects of chalcogen atom substitution on the optoelectronic and charge-transport properties in picene-type  $\pi$ -systems. *Chem. Commun.* **2017**, *53*, 3814–3817.